SOURCE
DATA

TRANSPARENT
PROCESS

THE
EMBO
JOURNAL

# Rabl2 GTP hydrolysis licenses BBSome-mediated export to fine-tune ciliary signaling

Shichao Duan[1,2,3,†], Hao Li[1,2,†], Yirong Zhang[1,2,†], Suming Yang[1,2], Yawen Chen[1,2], Benhua Qiu[1,2], Cheng Huang[1,2], Juan Wang[1,2], Jinsong Li[1,2], Xueliang Zhu[1,2,4,*] & Xiumin Yan[1,**]

## Abstract

Cilia of higher animals sense various environmental stimuli. Proper ciliary signaling requires appropriate extent of BBSome-mediated export of membrane receptors across ciliary barrier transition zone (TZ) through retrograde intraflagellar transport (IFT) machinery. How the barrier passage is controlled, however, remains unknown. Here, we show that small GTPase Rabl2 functions as a molecular switch for the outward TZ passage. Rabl2-GTP enters cilia by binding to IFT-B complex. Its GTP hydrolysis enables the outward TZ passage of the BBSome and its cargos with retrograde IFT machinery, whereas its persistent association leads to their shedding from IFT-B during the passing process and consequently ciliary retention. *Rabl2* deficiency or expression of a GTP-locked mutant impairs the ciliary hedgehog signaling without interfering with ciliation and respectively results in different spectrums of mouse developmental disorders. We propose that the switch role of Rabl2 ensures proper turnover of the BBSome and ciliary membrane receptors to fine-tune cilia-dependent signaling for normal embryonic development and organismic homeostasis.

## Introduction

Cilia function as antennae to detect a wide variety of environmental stimuli including light, odorants, and biological ligands and transduce the signals into the cell bodies to trigger cellular and organismic responses. Accordingly, many transmembrane receptors, including approximately two dozens of G protein-coupled receptors (GPCRs), have been reported to reside in cilia, and ciliary signaling is critical for embryonic development and organism sense such as vision, olfaction, and appetite (Berbari *et al*, 2009; Goetz & Anderson, 2010; Hilgendorf *et al*, 2016; Siljee *et al*, 2018). For instance, two ciliary GPCRs, Smoothened (Smo) and Gpr161, function in the hedgehog (Hh) signaling pathway critical for vertebrate embryonic development and homeostasis (Briscoe & Therond, 2013; Bangs & Anderson, 2017; Kong *et al*, 2019). Mammalian Hh pathway operates mainly by controlling *Gli1* expression through two paralogous transcriptional regulators, Gli2/3 (Hui *et al*, 1994; Hui & Angers, 2011; Niewiadomski *et al*, 2019). In the absence of Hh, ciliary Gpr161 mainly promotes the partial proteolytic processing of Gli3 into transcription repressor (Gli3-R). In the presence of Hh, the ligand binds to its membrane receptor Patched, resulting in ciliary entry of Smo and the retrieval of ciliary Patched and Gpr161 to enhance Gli activator (Gli-A, mainly Gli2-A) production at the ciliary tip. Gli-A then enters the nucleus to activate *Gli1* expression. Gli1 expressed to high levels thereby activates its downstream genes to eventually trigger cellular responses (Briscoe & Therond, 2013; Mukhopadhyay *et al*, 2013; Pal *et al*, 2016; Bangs & Anderson, 2017; Kong *et al*, 2019). Defects in Hh signaling lead to developmental disorders including midgestation lethality, defective neural patterning and neural tube closure, and polydactyly (Hui & Joyner, 1993; Goetz & Anderson, 2010; Briscoe & Therond, 2013; Bangs & Anderson, 2017; Hwang *et al*, 2018).

Proper turnover of ciliary signaling components, including membrane receptors, is physiologically important. As the ciliary base contains diffusion barriers such as the transition zone (TZ), a train-like intraflagellar transport (IFT) machinery powered by molecular motors associated with their accessory complexes IFT-A and IFT-B, is responsible for shuttling many ciliary components into and out of cilia (Nakayama & Katoh, 2018). Although membrane proteins can enter cilia by diffusion, their removal depends on retrograde IFT, in which BBSome, an octameric protein complex formed by Bardet–Biedl syndrome (BBS) proteins Bbs1, -2, -4, -5, -7, -8, -9,

1  State Key Laboratory of Cell Biology, Shanghai Institute of Biochemistry and Cell Biology, Center for Excellence in Molecular Cell Science, Chinese Academy of Sciences, Shanghai, China
2  University of Chinese Academy of Sciences, Beijing, China
3  Department of Pathology, First Affiliated Hospital of Zhengzhou University, Zhengzhou, China
4  School of Life Science, Hangzhou Institute for Advanced Study, University of Chinese Academy of Sciences, Hangzhou, China
   *Corresponding author (lead contact). Tel: +86 21 54921406; Fax: +86 21 54921011; E-mail: xlzhu@sibcb.ac.cn
   **Corresponding author. Tel: +86 21 54921404; E-mail: yanx@sibcb.ac.cn
   †These authors contributed equally to this work

and -18, functions as an adaptor between the GPCRs and IFT-B (Ye et al, 2013; Milenkovic et al, 2015; Mourao et al, 2016; Nachury, 2018; Ye et al, 2018). Disruption of the BBS proteins leads to ciliary accumulation of membrane receptors, abnormal signal transduction, and ciliopathy (Nishimura et al, 2004; Seo et al, 2011; Tadenev et al, 2011; Zhang et al, 2013). Interestingly, recent single-molecule studies reveal that significant fractions of GPCRs are recycled back after reaching TZ through retrograde IFT (Nachury, 2018; Ye et al, 2018). How the fate of recycle or removal is regulated and its physiological importance, however, remain unclear.

The Rab family of small GTPases functions as a molecular switch in membrane trafficking by cycling between the GTP-bound active and the GDP-bound inactive states (Stenmark, 2009). Rabl2 is a Rab-like small GTPase lacking membrane association property (Kanie et al, 2017; Blacque et al, 2018). Human cells possess two highly homologous and redundant paralogues, RABL2A and RABL2B. Depletion of both paralogues in RPE1 cells impairs ciliogenesis (Kanie et al, 2017). In the small portion of RABL2-deficient RPE1 cells still forming cilia, 20–30% of the IFT-B particles relative to those in wild-type cilia are detected (Kanie et al, 2017). RABL2 is capable of self-activation into GTP-binding form, and RABL2-GTP is proposed to stay at the ciliary base to capture IFT-B and trigger the ciliary entry of IFT-B, followed by its rapid inactivation through GTP hydrolysis (Kanie et al, 2017). Although exogenously expressed RABL2B$^{Q80L}$, a GTP-locked mutant, displays ciliary shaft localization, this has been attributed to artifact of the mutant (Kanie et al, 2017). Accordingly, its overexpression-induced ciliary accumulations of BBS4, GPR161, and serotonin receptor 6 (HTR6) are attributed to their enhanced ciliary entry (Kanie et al, 2017; Nishijima et al, 2017; Dateyama et al, 2019). There is only one murine Rabl2, whose deficiency results in BBS-like phenotypes polydactyly and retina degeneration (Kanie et al, 2017).

In this study, we show that Rabl2 is dispensable for IFT-B entry and ciliation in mice but enters cilia to function as a molecular switch to control the BBSome-mediated outward TZ passage for proper ciliary signaling.

# Results

## Rabl2-deficient mice display ciliopathy-like phenotypes but normal ciliation

We independently identified Rabl2 as a cilium-related gene from our cDNA array analysis using mouse tracheal epithelial cells (mTECs) cultured at an air-liquid interface (ALI) to induce multiciliogenesis (Xu et al, 2015) and confirmed the upregulation of Rabl2 during the multicilia formation (Fig 1A). Consistently, Rabl2 was highly expressed in cilia-enriched tissues such as the trachea, lung, oviduct, and testis (Fig 1B).

We used the same knockout mouse line as Kanie and colleagues did (Kanie et al, 2017) and confirmed that Rabl2 was downregulated in Rabl2$^{+/-}$ mice and undetectable in Rabl2$^{-/-}$ mice (Fig 1C and D). Similarly, the Rabl2$^{-/-}$ mice were born at the expected Mendelian ratio of genotypes, with 57% of them (n = 151) displaying polydactyly with the preaxial duplication of digit 1 in one or both sides of the hind limbs, and underwent retinal degeneration (Fig EV1A–D) (Kanie et al, 2017). Furthermore, we found that Rabl2$^{-/-}$ male

mice displayed infertility and defective sperm motility; they also outweighed their wild-type littermates from after 2 months of age (Fig EV1E–G).

In sharp contrast to RABL2 (Kanie et al, 2017; Nishijima et al, 2017; Dateyama et al, 2019), however, Rabl2 deficiency did not impact formations and morphologies of both monocilium and multicilia in tissues or cultured mouse ependymal cells (mEPCs) and mouse embryonic fibroblasts (MEFs; Fig 1E–J). Cilia length appeared to be slightly reduced when measured with MEFs (2.3 ± 0.6 μm vs. 2.5 ± 0.7 μm in wild-type MEFs; Fig 1J). Consistent with previous reports (Kanie et al, 2017; Nishijima et al, 2017; Dateyama et al, 2019), Rabl2 was enriched at the distal appendage (or transition fiber) of the basal body in primary cilia. The same localization was observed in multicilia as well (Figs 1G and I, and EV2).

Ciliogenesis is highly dependent on IFT-B-mediated anterograde IFT (Ishikawa & Marshall, 2011; Nakayama & Katoh, 2018). Although human RABL2 has been proposed to be critical for IFT-B entry into cilia (Kanie et al, 2017; Nishijima et al, 2017), the normal ciliation of Rabl2$^{-/-}$ cells (Fig 1E–J) suggested that murine Rabl2 was dispensable for the anterograde IFT. Indeed, IFT-B components Ift81 and Ift57 displayed normal distributions in the Rabl2-deficient MEFs (Fig 1K and L).

## Rabl2 is a regulator of Hh signaling

As the polydactyly phenotype of the Rabl2$^{-/-}$ mice (Fig 1A and B) (Kanie et al, 2017) strongly suggests defects in Hh signaling (Hui & Joyner, 1993; Briscoe & Therond, 2013; Bangs & Anderson, 2017; Tickle & Towers, 2017), we performed detailed analyses. When ciliated MEFs were treated with the Smo agonist SAG (Chen et al, 2002), Smo became similarly accumulated in the ciliary shaft in both Rabl2$^{+/+}$ and Rabl2$^{-/-}$ MEFs (Fig 2A). The SAG-induced accumulation of Gli2 at the ciliary tip (Santos & Reiter, 2014), however, decreased by 2.3-fold in the Rabl2$^{-/-}$ MEFs (Fig 2B), suggesting reduced formation of the Gli2 activator (Kong et al, 2019). Consistently, the upregulation of Gli1 was markedly reduced in the Rabl2$^{-/-}$ MEFs as compared to the Rabl2$^{+/+}$ or Rabl2$^{+/-}$ MEFs (Fig 2C). These results indicate attenuated Hh signaling (Kong et al, 2019) in the Rabl2$^{-/-}$ cells.

As the production of the Gli3 repressor (Gli3-R) is critical for the limb formation (Wang et al, 2000; Tickle & Towers, 2017), we examined whether its levels were altered in the limb bud of Rabl2$^{-/-}$ mouse embryos. We isolated hind limb bud tissues from E11.5 mouse embryos and examined the Gli3R levels relative to those of full-length Gli3 (Gli3-FL) by immunoblotting. The Gli3 FL/R ratio increased in the Rabl2$^{-/-}$ limb bud as compared to the Rabl2$^{+/+}$ or Rabl2$^{+/-}$ limb buds (Fig 2D), suggesting reduced production of Gli3-R. Similar results were obtained using whole E10.5 embryos (Fig 2E).

## GTP-locked mutant Rabl2$^{Q80L}$ enters ciliary shaft to repress the retrieval of GPR161 and SMO

To verify whether Rabl2 regulated Hh signaling by influencing the turnover of its ciliary GPCRs, we created a GTP-locked mutant Rabl2$^{Q80L}$ and a GDP-locked mutant Rabl2$^{S35N}$ and overexpressed them in human RPE1 cells for a better comparison with previous

publications (Fig 3A) (Kanie *et al*, 2017; Nishijima *et al*, 2017; Dateyama *et al*, 2019). Compared with RABL2B[S35N] (Nishijima *et al*, 2017; Dateyama *et al*, 2019), Rabl2[S35N] displayed similar weak ciliary base localization but did not significantly repress ciliogenesis (Fig 3B–D). Similar to RABL2B[Q80L] (Kanie *et al*, 2017; Dateyama *et al*, 2019), Rabl2[Q80L] also displayed ciliary shaft localization and enhanced the ciliary localization of GPR161 (Fig 3B and E). When the ciliary export of GPR161 upon the activation of Hh signaling was examined by treating the cells with SAG (Mukhopadhyay *et al*, 2013; Pal *et al*, 2016), the ciliary GPR161 was completely removed in the cells expressing GFP-Rabl2 or GFP-Rabl2[S35N] but persisted in those expressing GFP-Rabl2[Q80L] (Fig 3E).

To clarify whether the ciliary retention of GPR161 after the SAG treatment (Fig 3E) was due to excessive ciliary entry through the elevated anterograde IFT (Kanie *et al*, 2017; Dateyama *et al*, 2019) or reduced ciliary exit, we examined SMO, which enters cilia at low levels through diffusion, i.e., independently of the anterograde IFT, in the absence of HH signaling (Ye *et al*, 2013; Milenkovic *et al*, 2015). We observed that SMO strongly localized in the ciliary shaft of GFP-Rabl2[Q80L]-expressing RPE1 cells even without SAG treatment (Fig 3F). By sharp contrast, in RPE1 cells expressing GFP-tagged Rabl2 or Rabl2[S35N], ciliary SMO emerged only after the SAG treatment (Fig 3F). These results strongly suggest that the presence of Rabl2[Q80L] in the ciliary shaft represses the retrieval of ciliary GPCRs.
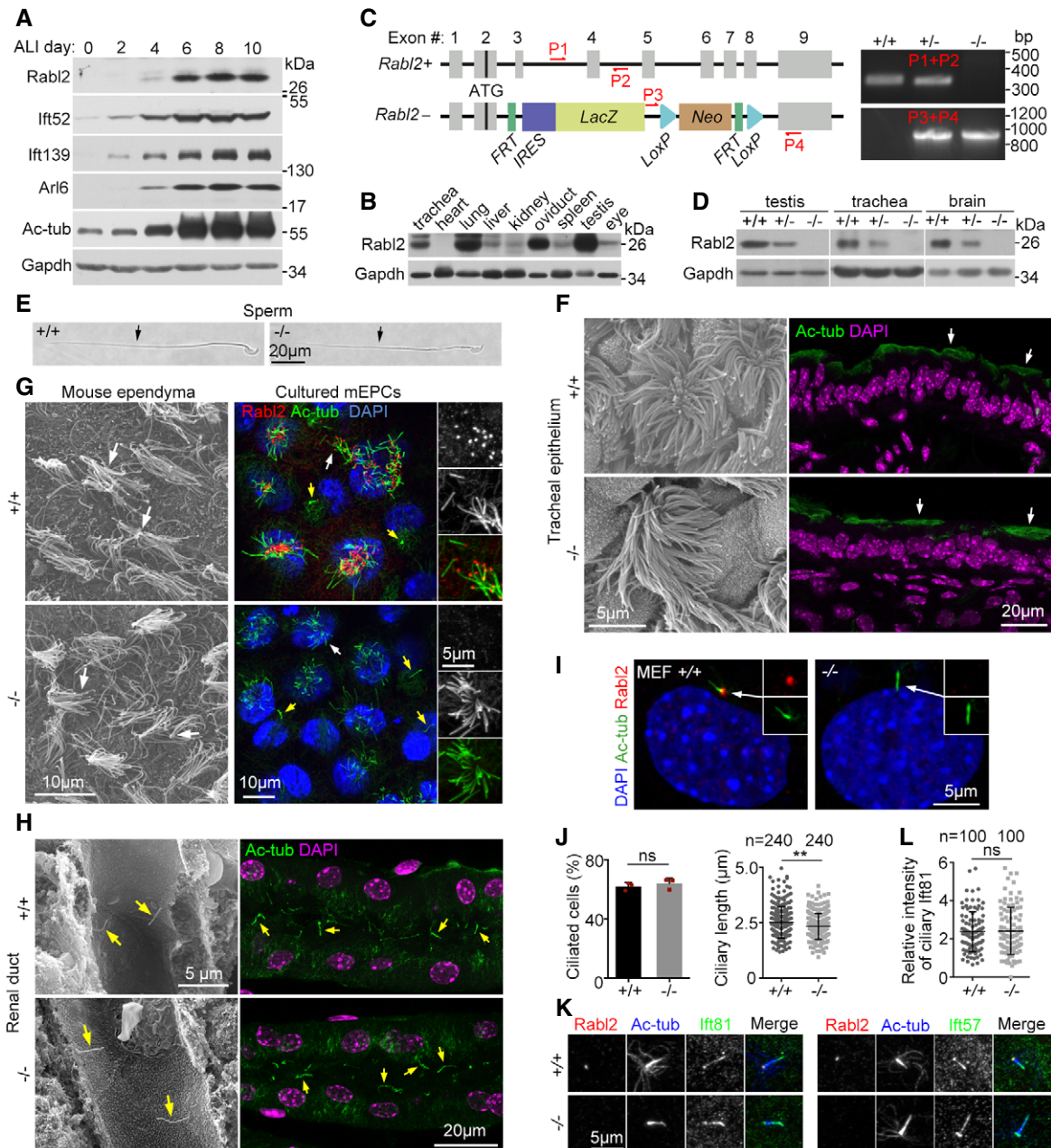


**Figure 1.**

◀ **Figure 1.  Murine Rabl2 is dispensable for ciliogenesis.**

A    Upregulation of Rabl2 during multiciliogenesis. Cultured mTECs were induced to undergo multicilia formation by growing at an air–liquid interface (ALI) for the indicated time and subjected to immunoblotting. Ift52, Ift139, Arl6, and acetylated tubulin (Ac-tub) served as ciliary markers. Gapdh served as the loading control.

B    Rabl2 levels in different tissues from 8-week-old mice.

C    *Rabl2* knockout strategy and representative genotyping PCR results using the indicated primers (P1–P4). *FRT*, flippase recognition target; *LacZ*, β-galactosidase gene; *Neo*, neomycin-resistant gene; *IRES*, internal ribosome entry site; *LoxP*, Cre recombinase recognition site.

D    Complete depletion of Rabl2 in tissues (from 8-week-old mice) upon its gene knockout.

E–H  Normal ciliary formation in representative bright-field (E), scanning electron (F, G, H), or immunofluorescent (F, G, H) micrographs of the indicated tissues (from 8-week-old mice) or cells. Cultured mEPCs were fixed at day 7 post-serum starvation. Ac-tub served as ciliary marker. DAPI labeled nuclear DNA. Typical cilia or flagella are indicated by arrows, in which yellow arrows denote primary cilia.

I, J  Normal ciliary formation of *Rabl2*$^{-/-}$ MEFs. MEFs derived from E12.5 mouse embryos were serum-starved for 48 h to induce primary cilia (I). Statistical results (J) were from three independent experiments. Ciliogenesis of at least 200 cells was scored in each experiment and condition. Ciliary lengths of 80 cells were measured in each experiment and condition, and the results of the same genotypes were pooled together.

K, L  *Rabl2* deficiency did not repress ciliary localization of IFT-B. Ciliated MEFs were immunostained for Ift81 and Ift57, two IFT-B subunits (K; see Fig 4F for diagram of IFT-B). Relative intensity of ciliary Ift81 (L), presented in arbitrary unit, was obtained by normalizing to that of corresponding Ac-tub. Four MEF strains prepared, respectively, from two embryos per genotype were used for quantification. 50 cilia were quantified from each MEF strain, and results of the same genotypes were pooled together.

Data information: Statistical results are presented as mean ± s.d. Student's *t*-test: ns, no significance; **$P < 0.01$.
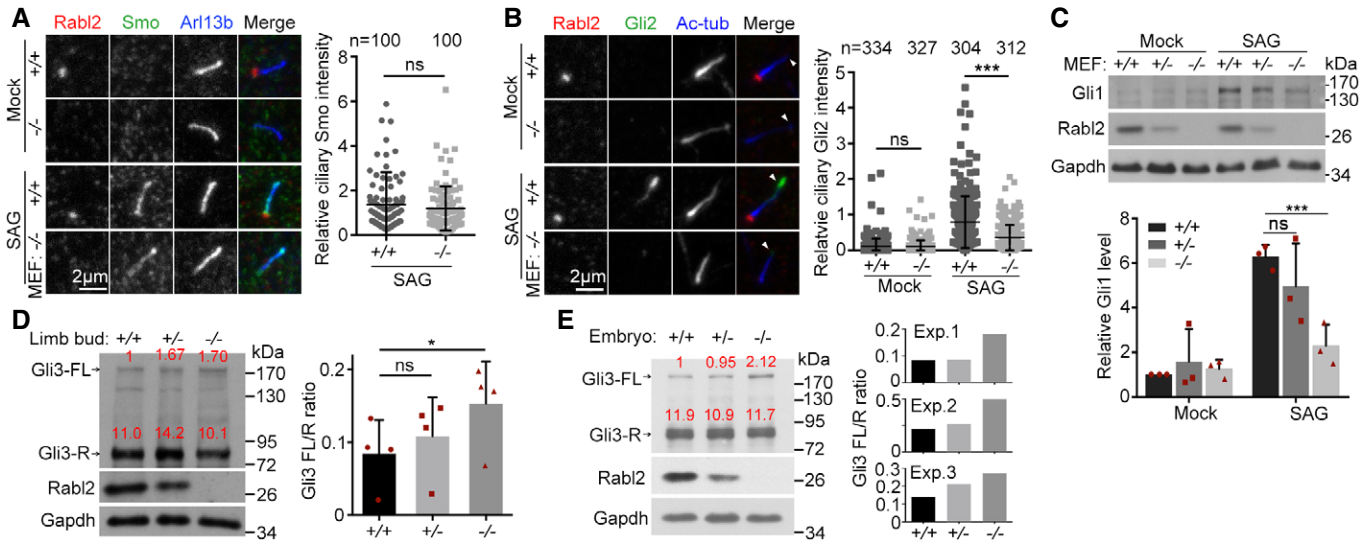Source data are available online for this figure.



**Figure 2.  *Rabl2* deficiency attenuates Hh signaling.**

A    Normal SAG-induced ciliary accumulation of Smo. MEFs serum-starved for 24 h were treated with DMSO (mock) or 100 nM SAG for an additional 24 h. Arl13b served as ciliary marker. We also examined Gpr161 but failed to observe specific immunofluorescent signals, though the antibody, prepared by using human GPR161, and recognized ciliary GPR161 well in human RPE1 cells (see Fig 3E). Quantification results were pooled from four MEF strains derived from two *Rabl2*$^{+/+}$ and two *Rabl2*$^{-/-}$ embryos.

B    Reduced Gli2 accumulation at the ciliary tip. MEFs were treated as in (A). Ac-tub served as ciliary marker. Arrowheads indicate ciliary tips. Quantification results were pooled from three independent experiments, each using MEFs from different embryos. At least 100 cells were scored in each experiment and condition.

C    Reduced Gli1 expression. MEFs treated as in (A) were lysed for immunoblotting. Gapdh served as the loading control. For quantification, three independent experiments were performed, each using MEFs from different embryos.

D, E  Increased Gli3 FL/R ratios in E11.5 hind limb buds and E10.5 mouse embryos. Relative band intensities of the full-length (FL) and the repressor (R) forms of Gli3 were quantified (red). FL/R ratios were from four different sets of limb bud preparations (D) and three different sets of embryo preparations (E).

Data information: Quantification results are presented as mean ± s.d. Student's *t*-test: ns, no significance; *$P < 0.05$; ***$P < 0.001$.
Source data are available online for this figure.

## Ciliary Rabl2$^{Q80L}$-caused inhibition of GPCR export impairs Hh signaling

As proper turnover of ciliary Gpr161 and Smo is critical for Hh signaling (Bangs & Anderson, 2017; Kong *et al*, 2019), we speculated that their abnormal accumulations in cells expressing Rabl2$^{Q80L}$ (Fig 3E and F) would impair the Gli-FL production and Gli1 expression. To verify this, we infected *Rabl2*$^{-/-}$ MEFs with lentivirus to express GFP, GFP-Rabl2, or GFP-Rabl2$^{Q80L}$ and treated the cells with SAG after inducing ciliogenesis. In contrast to GFP, GFP-Rabl2 restored the SAG-induced ciliary tip-accumulation of Gli2 as compared to the wild-type MEFs (Fig 3G). The
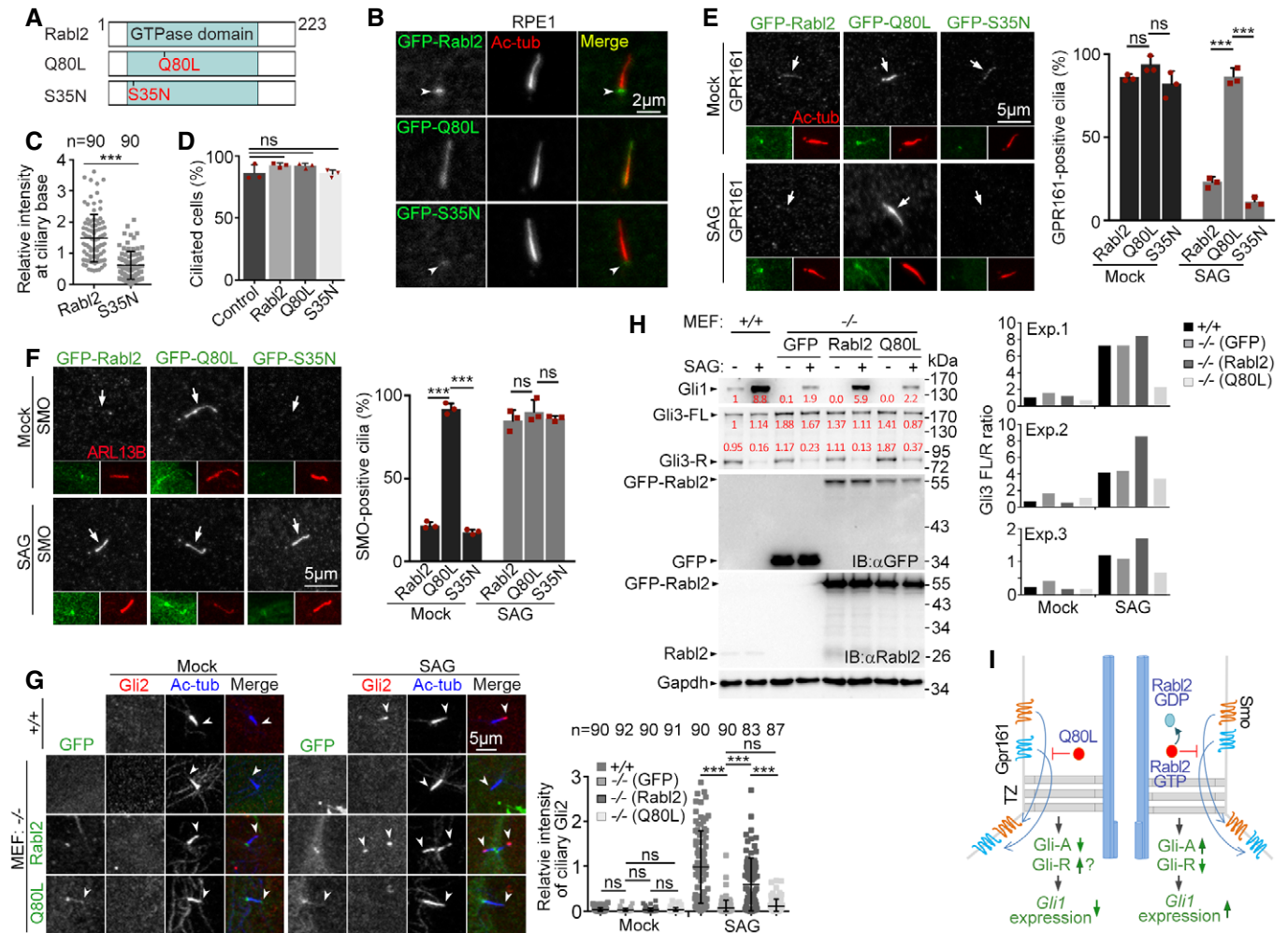
**Figure 3. Ciliary Rabl2^Q80L inhibits the export of SMO and GPR161 to repress Hh signaling.**

A    Diagrams of mouse Rabl2 and its GTP (Q80L)- or GDP (S35N)-locked mutants.

B    Subcellular localization of Rabl2 and mutants. RPE1 cells infected with adenovirus to express the GFP-tagged proteins were serum-starved for 48 h to induce ciliogenesis. Ac-tub served as ciliary marker. Arrowheads indicate ciliary base. The cells were used for quantifications in (C) and (D).

C    Reduced ciliary base localization of GFP-Rabl2^S35N as compared to GFP-Rabl2. Results from three independent experiments (*n* = 30 for each experiment and condition) were pooled together.

D    GFP-tagged Rabl2 and its mutants did not significantly affect ciliogenesis upon overexpression as compared to uninfected control cells. At least 104 cells were scored in each experiment and condition.

E    Rabl2^Q80L retained ciliary GPR161 after SAG stimulation. RPE1 cells infected as in (B) were serum-starved for 24 h, followed by DMSO (mock) or SAG treatment for 24 h. Arrows indicate cilia that are displayed in insets. At least 100 cilia were scored in each experiment and condition.

F    Rabl2^Q80L led to SAG-independent accumulation of ciliary Smoothened (SMO). RPE1 cells were treated as in (E). ARL13B served as ciliary marker. The white arrows point to positions of cilia. At least 100 cilia were scored in each experiment and condition.

G, H    Rabl2^Q80L inhibited Hh signaling. MEFs from *Rabl2^−/−* E12.5 embryos infected with lentivirus to express GFP, GFP-Rabl2, or GFP-Rabl2^Q80L were serum-starved for 24 h and treated with DMSO (mock) or 100 nM SAG for an additional 24 h. Uninfected MEFs from the wild-type littermate embryos served as the positive control. The samples were immunostained to examine ciliary Gli2 (G) or immunoblotted to examine levels of Gli1 and Gli3 (H). The white arrowheads (G) point to ciliary tips. Quantification results were from three independent experiments, each using MEFs from different *Rabl2*-deficient embryos. Gli2 intensities, presented in arbitrary unit, were measured from at least 22 cilia in each experiment and condition and pooled together. In the samples for immunoblotting (H), GFP-positive cells occupied 82.3% (GFP), 87.3% (GFP-Rabl2), and 81.2% (GFP-Rabl2^Q80L), respectively, when 260 cells in each sample were scored. Relative band intensities are shown in red.

I    A model summarizing the results in Fig 3 (left half) and speculating a switch role of endogenous Rabl2 for ciliary GPCR export and signaling, taking the Hh signaling as an example (right half). The GTP-locked Q80L mutant represses the export of ciliary Gpr161 and Smo, leading to reduced Gli-A and possibly increased Gli-R formations and accordingly attenuated *Gli1* expression. Endogenous ciliary Rabl2-GTP would similarly repress the export of Gpr161 and Smo until it was converted to GDP-binding form through GTP hydrolysis. Proper regulation of the GTP hydrolysis would therefore facilitate proper Hh signaling.

Data information: Quantification results are presented as mean ± s.d. Student's *t*-test: ns, no significance; ***P < 0.001.
Source data are available online for this figure.

effect of GFP-Rabl2$^{Q80L}$, however, was indistinguishable to that of GFP (Fig 3G).

Immunoblotting revealed that the levels of exogenous Rabl2 and Rabl2$^{Q80L}$ highly exceeded that of endogenous Rabl2 in wild-type MEFs (Fig 3H). Despite this, the SAG treatment still strongly induced Gli1 expression in the *Rabl2$^{-/-}$* MEFs expressing GFP-Rabl2; GFP-Rabl2$^{Q80L}$, however, displayed similar efficacy as GFP (Fig 3H). We also examined Gli3-R levels and observed that SAG induced Gli3-R reduction in all groups (Fig 3H). Quantification suggested that, in the absence of SAG, Gli3 FL/R ratios increased in the GFP groups as compared to the wild-type MEFs or the GFP-Rabl2 groups (Fig 3H). After SAG treatment, Gli3 FL/R ratios in the GFP-Rabl2$^{Q80L}$ groups displayed the least increase as compared to the other groups (Fig 3H). Taken together, we conclude that ciliary Rabl2$^{Q80L}$ inhibits Hh signaling (Fig 3I).

### Wild-type Rabl2-GTP enters cilia by binding to IFT-B and undergoes IFT

If wild-type Rabl2 never entered cilia as proposed previously for RABL2 (Kanie *et al*, 2017), the ciliary retention of GPCRs by Rabl2$^{Q80L}$ (Fig 3E and F) would be artificial effects. Alternatively, as both *Rabl2*-deficiency and Rabl2$^{Q80L}$ expression inhibited Hh signaling without affecting ciliogenesis (Figs 1–3 and EV1A), endogenous Rabl2-GTP might actually enter cilia to regulate the proper turnover of ciliary GPCRs through its GTP hydrolysis (Fig 3I). It has been shown that RABL2-GTP is specifically recruited to distal appendages by CEP19, where it binds to IFT-B (Kanie *et al*, 2017; Nishijima *et al*, 2017). The consistent localization of Rabl2 and Rabl2$^{Q80L}$ at distal appendages (Figs EV2 and EV3) suggested that Rabl2-GTP is recruited to distal appendages by the same mechanism to interact with IFT-B. Kanie and colleagues propose that IFT-B subsequently separates from RABL2 and enters cilia alone. Nevertheless, could Rabl2-GTP actually enter cilia together with IFT-B? To clarify this, we investigated whether we could detect wild-type Rabl2 in cilia.

As we usually needed to perform immunofluorescent staining to clearly visualize the ciliary GFP-Rabl2$^{Q80L}$ (Fig 3), we speculated that the ciliary Rabl2, if any, must be in very low levels. To boost detection sensitivity, we fused three tandem repeats of the super-bright NeonGreen (Shaner *et al*, 2013) to the wild-type Rabl2 (3NG-Rabl2) and readily observed punctate 3NG-Rabl2 autofluorescence in the shaft of both primary cilia of RPE1 cells and multicilia of cultured mEPCs (Fig 4A and B). More importantly, live imaging by total internal reflection fluorescence (TIRF) microscopy revealed clear anterograde and, less frequently and clearly, retrograde movements of 3NG-Rabl2 puncta in the primary cilia (Fig 4C and Movie EV1), with velocities of $0.97 \pm 0.14$ and $0.85 \pm 0.27$ μm/s, respectively, similar to those of reported IFT particles (He *et al*, 2014; Ishikawa & Marshall, 2015).

We next examined whether endogenous Rabl2 was present in purified cilia. As we were unable to purify enough primary cilia for this purpose, we purified multicilia from cultured mEPCs (Fig 4D) (Zheng *et al*, 2019). Our cilia preparation did not contain detectable Gapdh, Lamin B1, GM130, and Cep162 (Fig 4E), suggesting free of major cytosolic, nuclear, and membranous organelle contaminations and the basal body (Shelton *et al*, 1981; Nakamura *et al*, 1995; Wang *et al*, 2013). By contrast, known ciliary proteins, Ift81, Ift25, and acetylated tubulin, together with Rabl2, were clearly detected in

the purified cilia (Fig 4E). Therefore, Rabl2 enters cilia through anterograde IFT and also undergoes retrograde IFT.

Similar to RABL2B$^{Q80L}$ (Kanie *et al*, 2017; Nishijima *et al*, 2017), Rabl2$^{Q80L}$ strongly associated with IFT-B by binding to the IFT74-IFT81 heterodimer (Fig 4F–H). On the other hand, Rabl2$^{S35N}$ and even Rabl2 failed to display detectable interaction with IFT-B (Fig 4G and H). In sucrose gradient centrifugation of mouse testis lysates, IFT-B, marked by Ift74 and Ift81, was mainly enriched in fraction #16, whereas Rabl2 was abundant in low-MW fractions #4-#10 (Fig 4I). In parallel samples containing GTPγs, a non-degradable GTP analogue, however, a substantial portion of Rabl2, became co-fractionated with IFT-B (Fig 4I).

Therefore, we revise the model of Kanie and colleagues (Kanie *et al*, 2017) and propose that Rabl2-GTP enters cilia by tightly binding to IFT-B and undergoes both anterograde and retrograde IFT (Fig 4J). Dissociation is expected to occur when Rabl2-GTP is converted into Rabl2-GDP through GTP hydrolysis (Fig 4J) (Kanie *et al*, 2017; Nishijima *et al*, 2017).

### Rabl2$^{Q80L}$ induces robust ciliary accumulations of BBSome but not IFT components

To understand the mechanism underlying the ciliary GPCR export defects in the Rabl2$^{Q80L}$-expressing cells (Fig 3), we performed quantitative proteomic analyses on multicilia purified from mEPCs expressing GFP-tagged Rabl2$^{Q80L}$ or Rabl2 (Fig 5A and B) (Zhu *et al*, 2010; Zhang *et al*, 2019). Strikingly, while the abundances of IFT-B and IFT-A subunits were similar between the two samples, seven (Bbs1, -2, -4, -5, -7, -8, and -9) out of the eight known BBSome subunits (Mourao *et al*, 2016; Nakayama & Katoh, 2018) increased by more than sixfold in the Rabl2$^{Q80L}$ cilia sample (Fig 5B). Only Bbs18 was not detected by the mass spectrometry, possibly due to its small size (< 10 kDa). Arl6/Bbs3 and Lztfl1/Bbs17, BBS proteins involved in the coupling of the BBSome to ciliary membrane (Mourao *et al*, 2014; Nakayama & Katoh, 2018) and IFT-B (Seo *et al*, 2011; Eguether *et al*, 2014; Jiang *et al*, 2016; Chou *et al*, 2019), respectively, displayed moderate increases (twofold). Immunoblotting validated the sample quality and the proteomic results (Fig 5C).

We next confirmed the effects in primary cilia of RPE1 cells by immunostaining. It is known that endogenous BBS proteins are hardly visible in cilia by immunostaining (Eguether *et al*, 2014; Liew *et al*, 2014). Indeed, BBS5, BBS7, and ARL6 were rarely detected in the ciliary shaft of RPE1 cells expressing GFP-Rabl2 or GFP-Rabl2$^{S35N}$, whereas ciliary LZTFL1 was only observed weakly in < 32 % of the cells on average (Fig 5D and E). Nevertheless, they were strongly located in the ciliary shaft of more than 81% of GFP-Rabl2$^{Q80L}$-positive RPE1 cells (Fig 5D and E). By contrast, IFT81 was generally positive in the cilia regardless of the GFP-tagged proteins (Fig 5D and E).

Therefore, Rabl2$^{Q80L}$ selectively causes ciliary accumulations of the BBSome and its adaptor proteins Arl6 and Lztfl1, but not IFT-A and IFT-B complexes.

### Ciliary Rabl2-GTP represses outward TZ passage of the BBSome and its cargos

To clarify whether the ciliary BBSome accumulation by the constitutively activated Rabl2 mutant was due to increased entry or
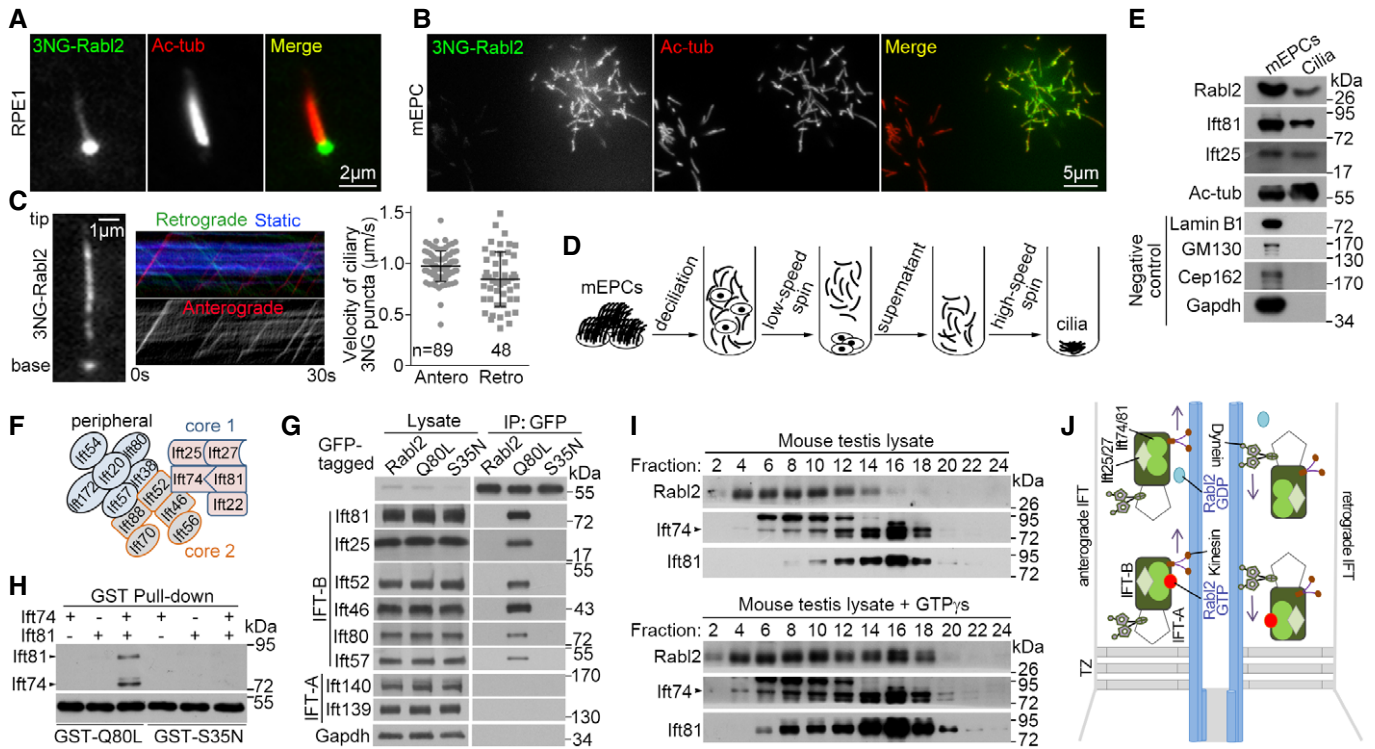
**Figure 4. Rabl2-GTP enters cilia through IFT.**

A, B    Wild-type Rabl2 was observed in the shaft of both primary cilium (A) and multicilia (B). Ciliated RPE1 cells (A) or mEPCs (B) expressing Rabl2 tagged with 3×mNeonGreen (3NG) were fixed at 48 h or day 7 post-serum starvation, respectively.

C        Ciliary 3NG-Rabl2 in living RPE1 cells underwent bidirectional IFT. The 1st frame and kymographs of a representative cilium (also see Movie EV1) are shown. Quantification results, presented as mean ± s.d, were measured from 34 cilia.

D, E    Detection of endogenous Rabl2 in purified multicilia. Multicilia purified from cultured mEPCs (D) were analyzed by immunoblotting (E). Ac-tub, Ift25, and Ift81 served as positive controls for cilia, whereas Lamin B1, GM130, Cep162, and Gapdh served as quality controls for the ciliary preparation to exclude major contaminations from the nucleus, Golgi, basal body, and cytosolic proteins, respectively. 1/400 of the mEPC lysate and 1/20 of the cilia lysate were loaded per lane.

F        Diagram of IFT-B. The core 1, core 2, and peripheral subcomplexes (Nakayama & Katoh, 2018) are depicted in different colors.

G        Rabl2$^{Q80L}$ strongly associated with IFT-B. GFP-Rabl2 or mutants stably expressed in NIH3T3 cells were immunoprecipitated with anti-GFP beads.

H        Rabl2$^{Q80L}$ interacted with the IFT74/81 heterodimer. FLAG-tagged Ift74 and Ift81 and GST-tagged Rabl2$^{Q80L}$ and Rabl2$^{S35N}$ expressed in *Escherichia coli* were mixed as indicated and pulled down with glutathione-conjugated beads. Antibodies to GST and FLAG were used for immunoblotting.

I         Association of endogenous Rabl2-GTP with IFT-B. Mouse testis lysates with or without 1 mM GTPγS were subjected to sucrose gradient ultracentrifugation. Fractions were collected from top (low MW) to bottom (high MW). Note the obvious enrichment of Rabl2 in fraction #16 in the presence of GTPγS.

J         A model delineating relationships between Rabl2 and IFT machinery. Rabl2-GTP enters cilia by binding to the Ift74-Ift81 heterodimer of IFT-B. After reaching the ciliary tip through anterograde IFT, it undergoes retrograde IFT toward the ciliary base. When its GTP is hydrolyzed into GDP during its IFT, the resultant Rabl2-GDP dissociates from IFT-B. The trafficking of IFT machinery continues in the absence of Rabl2.

Source data are available online for this figure.

decreased exit, we examined the ciliary exit rates of 3NG-Bbs5 in living RPE1 cells through fluorescence loss in photobleaching (FLIP; Fig 5F) (Liew *et al*, 2014). In the cells expressing RFP-Rabl2, ciliary 3NG-Bbs5 declined rapidly after the photobleaching, with an average half-life ($t_{1/2}$) of 294 ± 150 s (Fig 5F). In sharp contrast, ciliary 3NG-Bbs5 persisted for a longer time in cells expressing RFP-Rabl2$^{Q80L}$, with an average half-life of 546 ± 201 s (Fig 5F), indicating that ciliary Rabl2$^{Q80L}$ inhibits the BBSome export.

It is recently shown that two barriers, TZ and the periciliary barrier, gate the outward passage of membrane receptors at the ciliary base. The BBSome-mediated transport enables the passage through TZ but not the periciliary barrier (Nachury, 2018; Ye *et al*, 2018). We thus examined detailed ciliary protein localizations in RPE1 cells expressing GFP-Rabl2$^{Q80L}$ through super-resolution imaging. By using CEP290 or CEP162 as TZ markers, which localize to

the bottom of TZ (Fig EV3A) (Wang *et al*, 2013; Yang *et al*, 2015; Garcia-Gonzalo & Reiter, 2017), we confirmed that Rabl2$^{Q80L}$ and IFT-B (visualized through IFT81) distributed both on distal appendages and in the ciliary shaft (Fig EV3) (Kanie *et al*, 2017). BBSomes (visualized through BBS7), LZTFL1, SMO, and GPR161, however, distributed exclusively above TZ (Fig 5G and EV3C).

To further clarify whether the accumulation of the BBSome and its cargo proteins above TZ was due to their failure to cross TZ (Nachury, 2018; Ye *et al*, 2018) or be incorporated into the retrograde machinery at the ciliary tip (Eguether *et al*, 2014; Liew *et al*, 2014; Nakayama & Katoh, 2018), we monitored BBSome motility. Tracking the BBSome movement was somehow difficult in RPE1 cells, due to the lack of obvious consecutive movement of the 3NG-Bbs5 puncta, but feasible in mouse IMCD3 cells, which might be why the cells are commonly used to visualize mammalian BBSome

motility (Liew *et al*, 2014; Ye *et al*, 2018). In IMCD3 cells expressing either RFP-Rabl2 or RFP-Rabl2$^{Q80L}$, ciliary puncta of 3NG-Bbs5 or Ift27-GFP (representing IFT-B) underwent both anterograde and retrograde IFTs (Fig 5H and I and Movies EV2–EV5). IFT frequency of the puncta appeared to be slightly decreased in cilia of the Rabl2$^{Q80L}$-expressing cells, but only the reduction in the retrograde frequency of 3NG-Bbs5 puncta was statistically significant (Fig 5H and I). Comparing to RFP-Rabl2, RFP-Rabl2$^{Q80L}$ did not significantly alter IFT velocities of BBSomes or IFT-B (Fig 5H and I, and Movies EV2–EV5). Retrograde 3NG-Bbs5 puncta were observed to reach the base of Rabl2$^{Q80L}$-positive cilia (Fig 3H and Movie EV3), though the highly accumulated ciliary 3NG-Bbs5 precluded quantification on processivity of motile 3NG-Bbs5 puncta. When processivity of ciliary Ift27-GFP puncta was analyzed, we did not observe

significant changes between the Q80L and the Rabl2 groups (Fig 5I). Therefore, GTP-locked Rabl2 does not significantly alter ciliary IFT frequency, velocity, and processivity. Furthermore, the BBSome-containing retrograde IFT machinery can be assembled in the presence of Rabl2$^{Q80L}$ and actively reach the ciliary base. Taken together, these results suggest that Rabl2$^{Q80L}$, or Rabl2-GTP in physiological situations, specifically impair the outward TZ passage of the BBSome and its cargos.

## Outward TZ passage of BBSomes requires the release of ciliary Rabl2 from IFT-B

To understand how Rabl2-GTP blocks the BBSome passage through TZ, we screened for a Rabl2$^{Q80L}$-based mutant that entered cilia
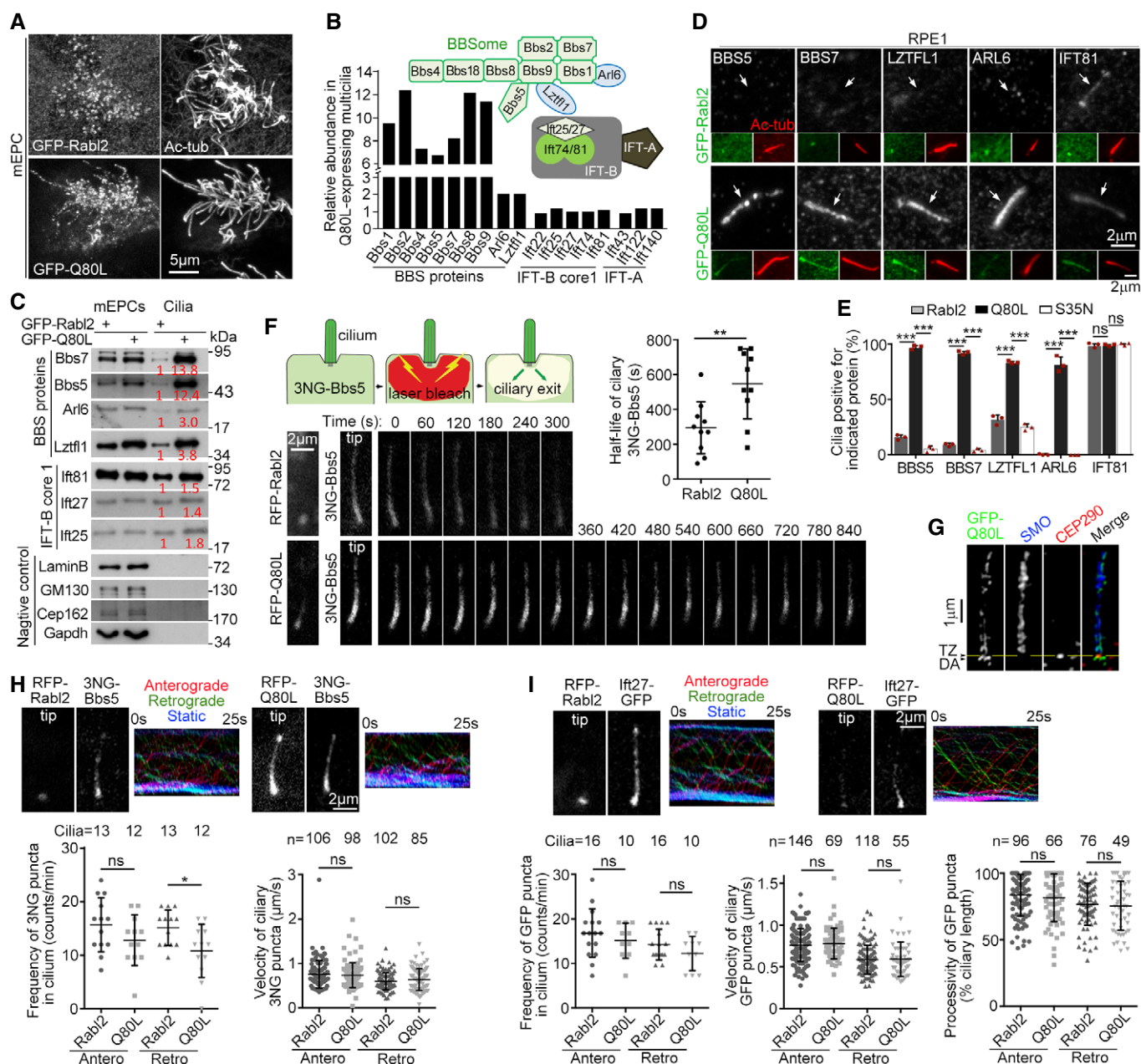


Figure 5.

◄

**Figure 5. GTP-locked Rabl2 represses outward passage of the BBSome and SMO through TZ.**

A    Rabl2$^{Q80L}$ localized in multicilia. Cultured mEPCs were infected with adenovirus to express GFP-Rabl2 or GFP-Rabl2$^{Q80L}$ at 24 h prior to and fixed at day 7 post-serum starvation.

B, C   Rabl2$^{Q80L}$ selectively induced ciliary accumulation of BBS proteins. Multicilia were purified from adenovirus-infected mEPCs harvested at day 10 and subjected to label-free quantitative (LFQ) mass spectrometric analyses (B) or immunoblotting (C). The abundance (B) is relative to LFQ intensities in the GFP-Rabl2 sample. Relationships among the BBS proteins, IFT-B, and IFT-A are depicted according to literature (Eguether *et al*, 2014; Nakayama & Katoh, 2018). Lztfl1 has been proposed to link BBSome to IFT-B through interaction with Ift27 (Eguether *et al*, 2014). Lamin B1, GM130, Cep162, and Gapdh served as quality controls for the ciliary preparations (C). The values in red are relative band intensities. 1/400 of the mEPC lysates and 1/20 of the cilia lysates were loaded per lane.

D, E   Ciliary accumulation of BBS proteins in Rabl2$^{Q80L}$-expressing RPE1 cells. The white arrows (D) point to positions of cilia. Quantification results (E) were from three independent experiments. At least 100 GFP-positive cells were scored in each experiment and condition.

F    FLIP assays revealed that ciliary Rabl2$^{Q80L}$ impaired BBSome export. RPE1 cells co-expressing 3NG-Bbs5 with RFP-Rabl2$^{Q80L}$ or RFP-Rabl2 were serum-starved to induce ciliogenesis. Photobleaching of 3NG in cells around the ciliary base was performed at $t = 0$ s as illustrated. Ciliary 3NG autofluorescence in the living cells was imaged at 30-s intervals after a snapshot for RFP. Images of representative cilia and half-life ($t_{1/2}$) of 10 cilia from one typical set of experiments are shown.

G    Ciliary SMO was accumulated above the transition zone (TZ; yellow line) in RPE1 cells expressing GFP-Rabl2$^{Q80L}$. Images were acquired through 3D-SIM. CEP290 served as TZ marker. DA, distal appendage. Also see Fig EV3.

H, I   BBSomes and IFT-B were able to reach the ciliary base through retrograde IFT in the presence of Rabl2$^{Q80L}$. Ciliary 3NG-Bbs5 (H) or Ift27-GFP (I) in IMCD3 cells co-expressing RFP-Rabl2 or RFP-Rabl2$^{Q80L}$ was live imaged at 4 fps. Snapshots for the ciliary RFP proteins, the first frames from Movies EV2–EV5, corresponding kymographs, and quantification results from the indicated numbers of cilia are presented. For processivity analysis (I), only traceable puncta were scored.

Data information: Data are presented as mean ± s.d. Student's *t*-test: ns, no significance; *$P < 0.05$; **$P < 0.01$; ***$P < 0.001$.
Source data are available online for this figure.

---

without causing BBSome accumulation and identified the Rabl2$^{D73GQ80L}$ double mutant. Similar to Rabl2$^{Q80L}$, GFP-Rabl2$^{D73GQ80L}$ localized in primary cilia of RPE1 cells without affecting the efficiency of ciliogenesis (Fig 6A). It underwent anterograde (0.94 ± 0.12 μm/s) and retrograde (0.72 ± 0.15 μm/s) IFT in the living cells (Fig 6B and Movie EV6). Rabl2$^{D73GQ80L}$, however, did not induce ciliary accumulation of BBS proteins (Fig 6C and D). Nor did it induce ciliary SMO accumulation in the absence of SAG or retain ciliary GPR161 upon SAG stimulation (Fig 6E and F). In comparison, GFP-tagged Rabl2$^{D73G}$, a mutant that causes infertility and obesity in mice (Lo *et al*, 2012; Lo *et al*, 2016), localized at the basal body in RPE1 cells (Fig EV4A). It also did not affect ciliogenesis, induce ciliary accumulation of BBSome and SMO, or alter the ciliary translocation of SMO in response to SAG treatment (Fig EV4).

Fluorescence loss in photobleaching assays confirmed that RFP-Rabl2$^{D73GQ80L}$ did not repress the ciliary exit of 3NG-Bbs5 as compared to RFP-Rabl2$^{Q80L}$ (Fig 6G). The average half-life of ciliary 3NG-Bbs5 in the RFP-Rabl2$^{D73GQ80L}$-expressing cells, 333 ± 151 s, was comparable to that in the RFP-Rabl2-expressing cells (Fig 6G vs. Fig 5F). Compared with Rabl2$^{Q80L}$, Rabl2$^{D73GQ80L}$ displayed a markedly reduced association with IFT-B (Fig 6H), suggesting that it is prone to dissociation from IFT-B in the ciliary shaft to achieve a similar effect as the GTP hydrolysis of Rabl2-GTP on the TZ passage of the BBSome and its cargos together with the IFT machinery (Fig 6I). Accordingly, persistent binding of Rabl2$^{Q80L}$ or Rabl2-GTP to IFT-B results in shedding of the BBSome and its cargos during the TZ passing process and thus their accumulation in the ciliary shaft (Fig 6I).

## Rabl2$^{Q80L}$ expression in mice closely resembles *Ift27* deficiency

As *in vitro* assays including gradient centrifugation are unable to detect the complex formation between BBSome and IFT-B (Seo *et al*, 2011), probably due to autoinhibition of BBSome in solution (Chou *et al*, 2019), so far proteins involved in their coupling, Lztfl1 on the BBSome side and Ift27 on the IFT-B side, are identified through genetic approaches (Eguether *et al*, 2014). To verify that the BBSome and its cargos were indeed prone to shedding from the

Rabl2-GTP-bound IFT-B, we likewise utilized genetic approach by generating *Rabl2$^{Q80L}$* knock-in (KI) mice using template-mediated repair of Cas9-induced DNA mutation (*mt*) in zygotes (Fig 7A) (Wu *et al*, 2013). Of 125 neonatal F1 mice subjected to genotyping, nine mice displayed uniform "TT" mutations in the PCR products indicative of homozygous *Rabl2$^{KI/KI}$* mutations (Fig 7B and C). Three mice were still wildtype, whereas the remaining 113 mice showed mixed peaks in sequencing that could be interpreted as heterozygous mice of varying genotypes or chimeric mice (Figs 7C and EV5). As our genotyping method could not distinguish heterozygous mice from chimeric mice, we only examined viability for this population (Fig 7C).

Compared with an overall death rate of 34.4% for the 125 mice within the day of birth, the death rate for the *Rabl2$^{KI/KI}$* mice was 88.9% (Fig 7C), indicating that mice expressing only Rabl2$^{Q80L}$ are prone to neonatal death. The death rate (53.4%) for the *Rabl2$^{KI/mt}$* mice was threefold over the rate (17.6%) for the *Rabl2$^{mt/x}$* mice, suggesting a dose-dependent lethality of Rabl2$^{Q80L}$. Furthermore, all the *Rabl2$^{KI/KI}$* mice examined (7/7) contained duplex kidney on either one side (6/7) (Fig 7D) or both sides (1/7), though their ciliary formation in renal ducts was normal (Fig 7E). We did not observe obvious polydactyly in them. We also started to maintain the F1 *Rabl2$^{KI/+}$* mice and found that, among the first batch of their seven F2 neonatal progeny, three wild-type and two *Rabl2$^{KI/+}$* puppies were viable with normal kidneys. By contrast, the two *Rabl2$^{KI/KI}$* littermates died after a natural birth and respectively possessed single and double duplex kidneys, confirming the phenotypes of *Rabl2$^{KI/KI}$* mice (Fig 7C and D) and also indicating that the gene editing-produced F1 *Rabl2$^{KI/+}$* mice are indeed heterozygotes and capable of germline transmission.

We examined cultured mEPCs from *Rabl2$^{KI/KI}$* brain tissues and found that the endogenous Rabl2$^{Q80L}$ entered the shaft of both multicilia and primary cilia (Fig 7F and G). Consistent with the effect of exogenous Rabl2$^{Q80L}$ (Fig 5), the endogenous Rabl2$^{Q80L}$ also induced ciliary BBSome accumulation suggested by the strong Bbs5 staining (Fig 7F and G). Smo was also accumulated in the *Rabl2$^{KI/KI}$* primary cilia in the absence of SAG treatment (Fig 7G). These results further strengthen the idea that the GTP hydrolysis of
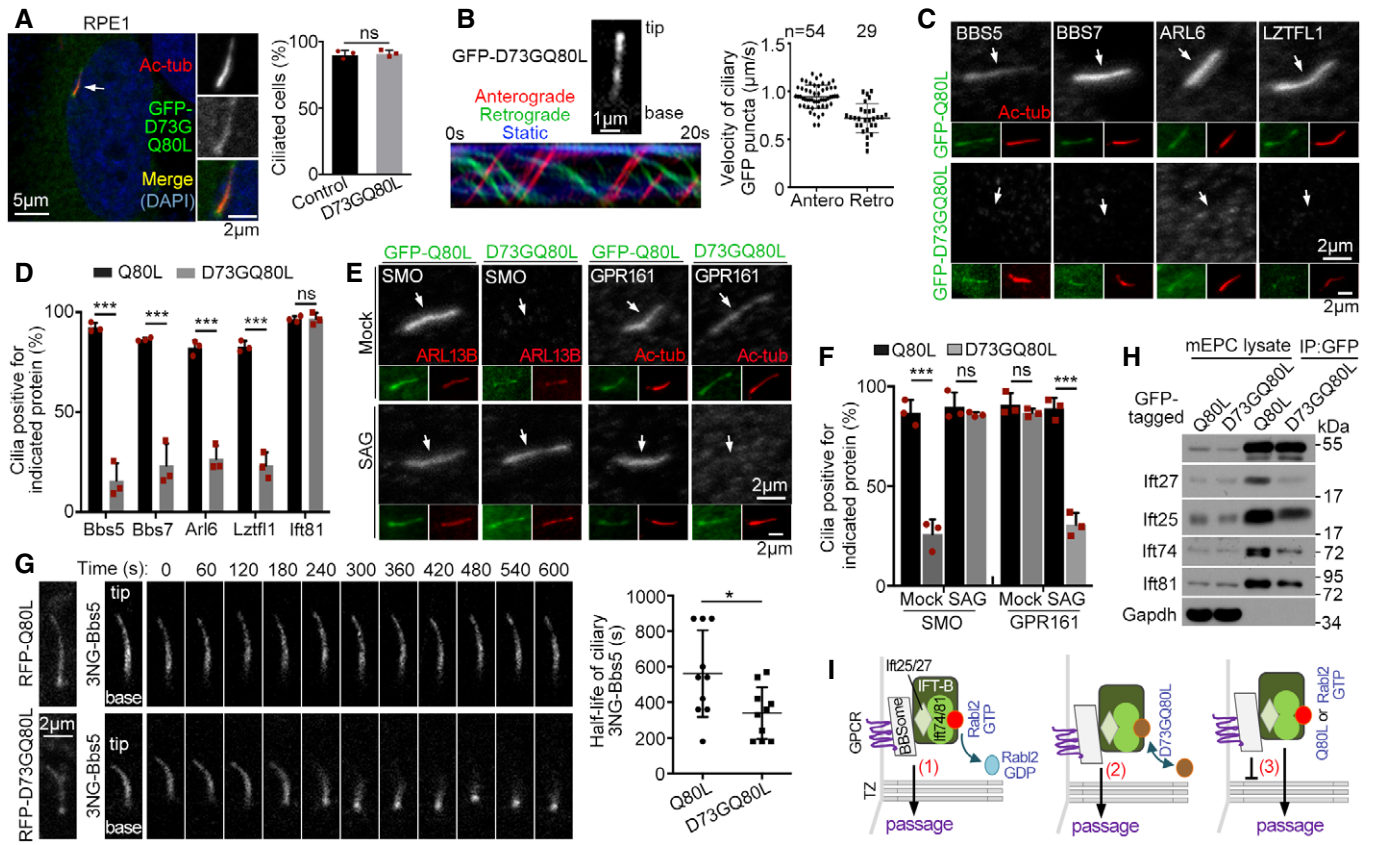
**Figure 6. TZ passage of ciliary BBSome-GPCR requires dissociation of Rabl2 from IFT-B.**

A    Rabl2$^{D73GQ80L}$ localized in the ciliary shaft and did not affect ciliogenesis efficiency. RPE1 cells infected with adenovirus to express GFP-Rabl2$^{D73GQ80L}$ were serum-starved for 48 h. The white arrow denotes the cilium shown in insets. Quantification results were from three independent experiments. Uninfected RPE1 cells served as control. At least 107 cells were scored in each experiment and condition.

B    Rabl2$^{D73GQ80L}$ underwent bidirectional IFT. Ciliary GFP-Rabl2$^{D73GQ80L}$ in RPE1 cells was live imaged at 5 fps. The 1$^{st}$ frame and kymograph of a representative cilium (also see Movie EV6) are shown. Velocities were quantified from 10 cilia.

C, D    Rabl2$^{D73GQ80L}$ did not induce ciliary accumulation of BBS proteins. Ciliated RPE1 cells expressing GFP-tagged Rabl2$^{Q80L}$ or Rabl2$^{D73GQ80L}$ were immunostained (C). The white arrows (C) point to positions of cilia. In quantification results (D), at least 100 cells were scored in each experiment and condition.

E, F    Rabl2$^{D73GQ80L}$ did not repress ciliary translocation of SMO and GPR161. RPE1 cells expressing GFP-tagged Rabl2$^{Q80L}$ or Rabl2$^{D73GQ80L}$ were serum-starved for 24 h and treated with DMSO (mock) or SAG for an additional 24 h prior to immunostaining (E). The white arrows (E) point to positions of cilia. In quantification results (F), at least 100 cells were scored in each experiment and condition.

G    Ciliary Rabl2$^{D73GQ80L}$ did not repress the BBSome export. FLIP assays were performed in RPE1 cells co-expressing 3NG-Bbs5 with RFP-tagged Rabl2$^{Q80L}$ or Rabl2$^{D73GQ80L}$ as depicted in Fig 5F. Photobleaching was executed at $t = 0$. Quantification results on half-life ($t_{1/2}$) were from 10 cilia for each condition.

H    Rabl2$^{D73GQ80L}$ displayed an attenuated association with IFT-B as compared to Rabl2$^{Q80L}$. mEPCs infected with adenovirus to express GFP-Rabl2$^{Q80L}$ or Rabl2$^{D73GQ80L}$ were lysed and immunoprecipitated using anti-GFP beads. Gapdh served as the negative control.

I    A model delineating the effects of Rabl2 and mutants on the TZ passage of ciliary BBSome and its cargo GPCR: (1) In physiological conditions, the GTP hydrolysis of Rabl2-GTP results in Rabl2-free IFT-B capable of mediating the TZ passage of the BBSome and its cargos together with the retrograde IFT machinery; (2) Rabl2$^{D73GQ80L}$ dissociates from IFT-B to allow similar TZ passage; (3) The BBSome sheds from IFT-B in the presence of Rabl2$^{Q80L}$ or Rabl2-GTP during the passing process and is therefore blocked in the ciliary shaft with its cargos.

Data information: Quantification results are presented as mean ± s.d. Student's $t$-test: ns, no significance; *$P < 0.05$; ***$P < 0.001$.
Source data are available online for this figure.

IFT-B-bound Rabl2-GTP is key to the outward TZ passage of the BBSome and its cargos (Fig 7H).

Notably, the neonatal lethality, duplex kidney, normal ciliation, and ciliary accumulation of BBSome and GPCRs are also characteristic phenotypes of the *Ift27* null mice (Eguether *et al*, 2014; Desai *et al*, 2018). Ift27 is a Rab-like small GTPase (also termed Rabl4) stabilized by Ift25 through heterodimerization and also the essential subunit for the coupling of IFT-B to the

BBSome and its cargos (Fig 7H) (Bhogaraju *et al*, 2011; Keady *et al*, 2012; Eguether *et al*, 2014; Blacque *et al*, 2018; Nakayama & Katoh, 2018). *Ift25*-deficient mice also show similar phenotypes except for the less extent of neonatal death (Keady *et al*, 2012; Desai *et al*, 2018). Therefore, the Rabl2$^{Q80L}$ expression is largely equivalent to the depletion of Ift27. More importantly, the high similarity in mouse genetic models validates our proposed function of Rabl2 (Fig 7H).
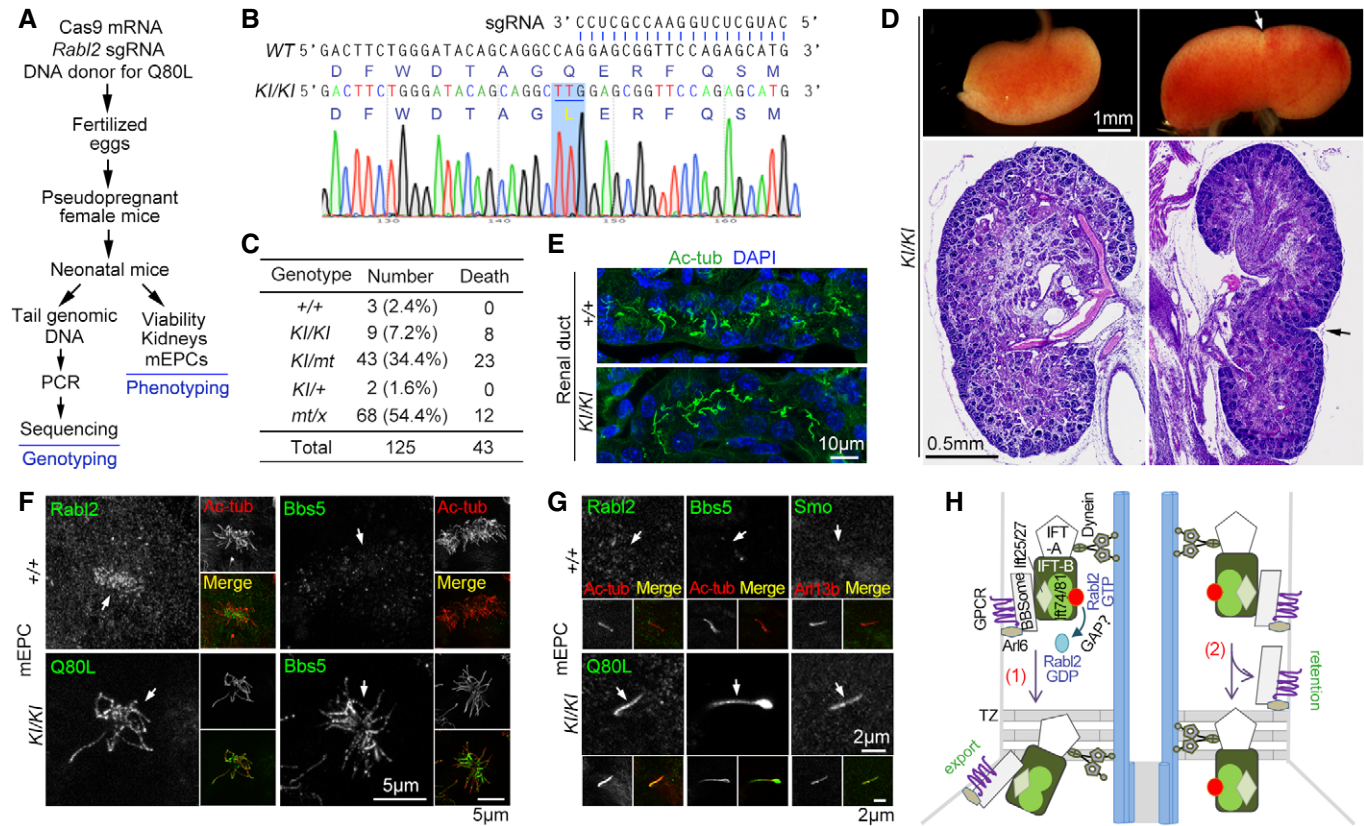
**Figure 7.  *Rabl2^Q80L* knock-in mice display neonatal death and duplex kidney that phenocopy *Ift27*-deficient mice.**

A  Experimental scheme for the knock-in (KI) mice production and characterization. The single-stranded DNA donor-mediated repair of the Cas9-induced *Rabl2* DNA breaks is expected to introduce the Q80L mutation in fertilized eggs or early embryos. Neonatal F1 mice were obtained through the cesarean section at E18.5. Genotyping was performed by directly sequencing the PCR products that covered the expected Cas9-cleavage region of *Rabl2*.

B  Representative sequencing results for *Rabl2^KI/KI* mice, shown with corresponding sequences for wildtype *Rabl2* and the 3′ end of the sgRNA. The TTG codon for the Q80L mutation is underlined.

C  Viability of neonatal mice in the day of birth after the cesarean section at E18.5. +, wildtype allele of *Rabl2*; *KI*, knock-in allele with Q80L mutation; *mt*, allele with Cas9-induced mutation; *x*, ambiguous allele. Refer to Fig EV5 for additional genotyping results. As these "heterozygous" mice might contain chimeric ones, the putative genotypes are used only for simplicity.

D  Morphologically normal and duplex kidneys of *Rabl2^KI/KI* mice. The whole kidneys were from a single mouse. The histological sections, stained with hematoxylin and eosin, were from different mice. Arrows point to the constriction of the duplex kidneys.

E  Renal ducts of *Rabl2^KI/KI* kidney displayed normal ciliary formation as compared to wildtype kidney. Nuclear DNA was stained with DAPI.

F, G  Endogenous Rabl2^Q80L entered ciliary shaft to repress the export of the BBSome (Bbs5) and its cargo GPCR (Smo). mEPCs cultured from *Rabl2^KI/KI* and wild-type neonatal mice were fixed at day 7 post-serum starvation. Anti-Rabl2 antibody was used to visualize Rabl2 and Rabl2^Q80L. Ac-tub or Arl13b served as ciliary marker. Representative micrographs of multicilia (F) and primary cilia (G) are shown. The white arrows point to positions of cilia.

H  A model delineating the switch role of ciliary Rabl2 in the BBSome-mediated GPCR turnover: (1) GTP hydrolysis induced presumably by a GTPase-activating protein (GAP) dissociates Rabl2 from IFT-B to enable a tight BBSome-IFT-B interaction in the retrograde IFT machinery for concomitant TZ passage; (2) Without the GTP hydrolysis, Rabl2-GTP (or Rabl2^Q80L) binds persistently to IFT-B, resulting in shedding of the BBSome and its cargos from the IFT machinery in the TZ passing process and accordingly their ciliary retention. See Discussion for details. For simplicity, kinesin motor is not illustrated.

# Discussion

In sharp contrast to human RABL2 (Kanie *et al*, 2017; Nishijima *et al*, 2017), murine *Rabl2* is largely dispensable for ciliogenesis and ciliary entry of IFT-B. *Rabl2* deficiency did not obviously interrupt the formation of either primary or motile cilia in tissues and cultured cells (Fig 1). The fact that *Rabl2*-deficient mice are viable (Fig EV1) (Kanie *et al*, 2017) is also consistent with this because severe ciliary defect is known to cause early embryonic lethality (Bangs & Anderson, 2017; Nakayama & Katoh, 2018). Furthermore, overexpression of wild-type Rabl2 or its GTP-locked (Q80L) or

GDP-locked (S35N) mutants in RPE1 cells also did not alter ciliogenic efficiency (Figs 3D and EV4A). As ciliary IFT-B is essential for anterograde IFT and, consequently, ciliary elongation, these observations already suggest that Rabl2 is unlikely critical for the ciliary entry of IFT-B. In agreement with this, ciliary Ift81 levels were similar between the wild-type and *Rabl2^−/−* MEFs (Fig 1K and L), and overexpression of Rabl2^Q80L did not significantly alter IFT frequencies of IFT-B (Fig 5I) or ciliary levels of IFT-B and IFT-A subunits (Figs 5B and EV3). Our current results, however, do not exclude the possibility that the interaction between Rabl2-GTP and IFT-B at distal appendages or transition fibers (Figs 3F–I and EV3) also

subtly facilitates the ciliary entry of IFT-B. RABL2 might become more important in this in evolution through the generation of two paralogous genes. Alternatively, as the *Chlamydomonas* orthologue is critical for flagella formation (Nishijima *et al*, 2017), evolution might somehow largely relieve murine Rabl2 of this role. In addition, it is also worth noting that studies on RABL2 are solely based on RPE1 cells. Results in other human cells, especially primary cells, still await future investigations. For simplicity, we take Rabl2 as the common name in the following discussion unless the human orthologue is specifically mentioned.

We demonstrated that Rabl2-GTP enters cilia to undergo antero-grade and retrograde IFT (Figs 3B, 4 and 6B; Movies EV1 and EV6). As the interaction of RABL2-GTP with CEP19 and the IFT74-IFT81 heterodimer is mutually exclusive (Nishijima *et al*, 2017), we revise the previous model (Kanie *et al*, 2017) to propose that the ciliary entry of Rabl2-GTP from distal appendages is triggered by IFT-B through direct interaction. Ciliary Rabl2 is undetectable through fluorescent microscopy even upon overexpression (Figs 1, EV2, 3, 5A, and EV3) (Kanie *et al*, 2017; Nishijima *et al*, 2017; Dateyama *et al*, 2019), unless tagged with super-bright fluorescent proteins such as 3NG (Fig 4A–C). By contrast, ciliary IFT-B components can be readily detected (Figs 1K and EV3) (Hirano *et al*, 2017; Kanie *et al*, 2017), indicating that only a small portion of IFT-B entering cilia is Rabl2-bound. Such a dependency on IFT-B also explains why the ciliary fluorescent intensity of exogenous $Rabl2^{Q80L}$ is always moderate (Figs 3, 5A, and EV3) (Kanie *et al*, 2017; Dateyama *et al*, 2019), even with its levels in cells markedly exceeding those of endogenous Rabl2 (Fig 3H, lanes 7–8 vs. lanes 1–2).

Our results suggest that Rabl2 functions as a switch for the BBSome-mediated export of ciliary signaling proteins such as GPCRs (Figs 5, 6 and 7F–H). As $Rabl2^{Q80L}$ did not strongly alter the IFT behaviors of IFT-B and BBSome (Fig 5H and I), the $Rabl2^{Q80L}$-induced accumulation of the BBSome and multiple GPCRs (Figs 5B–D, and 7F and G) (Kanie *et al*, 2017; Dateyama *et al*, 2019) above TZ (Figs 5G and EV3) is attributed to their shedding from the retrograde IFT machinery during the TZ passage (Fig 7H) (Nachury, 2018; Ye *et al*, 2018). As the accumulation effect of $Rabl2^{Q80L}$ was comprised by an additional mutation (D73G) that attenuated its interaction with IFT-B (Fig 6), dissociation of Rabl2-GTP from IFT-B through its GTP hydrolysis would similarly allow efficient TZ passage of the BBSome and its cargos (Fig 7H).

The switch role of Rabl2 appears to control the extent of the BBSome-mediated export of ciliary membrane receptors to fine-tune cilia-dependent signaling for normal embryonic development and organismic homeostasis. While ciliary Rabl2-GTP represses the GPCR export as suggested by the accumulation effect of $Rabl2^{Q80L}$ (Figs 3, 7G and H, and EV3) (Kanie *et al*, 2017; Dateyama *et al*, 2019), Rabl2 deficiency results in reduced levels of ciliary GPCRs (Dateyama *et al*, 2019). As both the Rabl2 deficiency and $Rabl2^{Q80L}$ expression impaired Hh signaling (Figs 2 and 3 and 7), a proper balance between the TZ export and the ciliary retention of Smo and Gpr161 is critical for optimal Hh signaling (Fig 7H). Accordingly, the polydactyly of *Rabl2*-deficient mice (Fig EV1A and B) (Kanie *et al*, 2017) and the neonatal lethality and duplex kidney of the $Rabl2^{KI/KI}$ mice (Fig 7C and D) may result from aberrant Hh signaling (Eguether *et al*, 2014; Tickle & Towers, 2017; Desai *et al*, 2018; D'Cruz *et al*, 2020). The retina degeneration, obesity, and male infertility of the *Rabl2*-deficient mice (Fig EV1C–G) (Kanie *et al*,

2017) and $Rabl2^{Mot/Mot}$ mice (Lo *et al*, 2012; Lo *et al*, 2016), whose etiology could be attributed to premature dissociation of ciliary $Rabl2^{D73G}$-GTP from IFT-B according to our results (Fig 6) to partly resemble *Rabl2* deficiency, also implicate abnormal ciliary signaling of other GPCRs (Forsythe & Beales, 2013; Hilgendorf *et al*, 2016).

The largely shared phenotypes between our $Rabl2^{KI/KI}$ mice (Fig 7A–G) and the *Ift27*-deficient mice (Eguether *et al*, 2014; Desai *et al*, 2018) appear to indicate that the ciliary Rabl2-GTP functions to counteract or repress Ift27 on IFT-B. Unlike many other IFT-B core subunits, mammalian Ift27 and Ift25 are dispensable for antero-grade IFT, ciliogenesis, and early embryo viability. Rather, the Ift25-Ift27 heterodimer functions in the coupling of the BBSome and its cargos to IFT-B for retrograde IFT to regulate ciliary signaling (Keady *et al*, 2012; Eguether *et al*, 2014; Bangs & Anderson, 2017; Nakayama & Katoh, 2018). The overall analogous phenotypes between the $Rabl2^{KI/KI}$ and the $Ift27^{-/-}$ mice, such as the neonatal death and duplex kidney, suggest that the accumulated ciliary BBSome and membrane receptors resulting from either the $Rabl2^{Q80L}$-induced shedding and the *Ift27* deficiency-resultant decoupling have similar influences on ciliary signaling, whereas the differential phenotypes, such as preaxial polydactyly observed in *Ift27*-deficient but not our $Rabl2^{KI/KI}$ mice, may be attributed to the difference in detailed mechanisms (Fig 7) (Eguether *et al*, 2014; Desai *et al*, 2018). As the duplex kidney is unlikely sufficient to cause the neonatal lethality, detailed examinations in the future are expected to reveal more defects in the $Rabl2^{KI/KI}$ mice, e.g., abnor-mal neural tube patterning observed in *Ift27*-deficient mice (Eguether *et al*, 2014). As both Rabl2-GTP (Fig 4H) (Kanie *et al*, 2017; Nishijima *et al*, 2017) and Ift27 (Lucker *et al*, 2010; Taschner *et al*, 2014; Nakayama & Katoh, 2018) bind to the Ift74-Ift81 hetero-dimer (Fig 7H), Rabl2-GTP may weaken the association of IFT-B with the BBSome by inducing conformational changes of Ift27. On the other hand, as small GTPases usually require GTPase-activating proteins (GAP) for rapid GTP hydrolysis (Blacque *et al*, 2018), a GAP might exist in cilia to specifically inactivate Rabl2-GTP. There-fore, further investigations are required to fully understand the regu-latory mechanisms underlying the BBSome-IFT-B interaction.

## Materials and Methods

### Plasmids

The mouse full-length cDNAs of *Rabl2* (NM_026817), *Ift27* (NM_025931), *Ift74* (NM_026319), *Ift81* (NM_009879), and *Bbs5* (NM_028084) were PCR amplified from mouse testis cDNAs. The full-length of *Rabl2* were, respectively, cloned into pLV-GFP-C1, pLV-RFP-C1, pGEX-4T-1, and pET-28a to express GFP-, RFP-, GST-, and His-tagged proteins. The point mutations of *Rabl2*, including $Rabl2^{S35N}$, $Rabl2^{Q80L}$, $Rabl2^{D73GQ80L}$, and $Rabl2^{D73G}$ were generated using site-directed mutagenesis. To generate the adenoviral plas-mids of *Rabl2* and its mutants, the PCR-amplified DNA fragments were subcloned into pYR-1.1 and a subsequent LR recombination reaction with pAd/Block-it-DEST was performed using LR Clonase II enzyme mix (11791020, Thermo Fisher). To construct the plasmids of $3{\times}mNeonGreen-Bbs5$ (3NG-Bbs5) and 3NG-Rabl2, the full-length DNA fragments of *Bbs5* and *Rabl2* were subcloned into pLV-mNeonGreen (modified from pLV vector carrying an insertion of

three tandem repeats of *mNeonGreen*). To express Ift27-GFP, the DNA fragment of *Ift27* was subcloned into pLV-GFP-C1. The DNA fragments of *Ift74* and *Ift81* were constructed into pFLAG-1 to express FLAG-tagged proteins in *Escherichia coli*. All constructs were verified by sequencing. The detailed information of plasmid constructs and used primers is listed in Appendix Table S1.

## Mice

All mice experiments were performed in accordance with protocols approved by the Institutional Animal Care and Use Committee of Shanghai Institute of Biochemistry and Cell Biology. Mice were selected solely based on genotypes.

*Rabl2^tm1(KOMP)Wtsi^* mice were purchased from the KOMP Repository (University of California Davis). Heterozygous offspring were intercrossed to generate *Rabl2^−/−^* mice. Genotyping was performed by PCR with genomic DNA extracted from mouse tails. The sequences of the PCR primers were 5′ TCCCTATCTG TATTGTTGTT CC 3′ (P1), 5′ ACCATTGATT CCTTGTCTCC 3′ (P2), 5′ ACACCTCC CC CTGAACCTGA AA 3′ (P3), and 5′ CTCAAGGGTT TGCATCATTC TCTCGG 3′ (P4).

*Rabl2^Q80L^* knock-in (*Rabl2^KI/KI^*) mice that endogenously expressed Rabl2^Q80L^ were generated using a CRISPR/Cas9 genome editing protocol as described previously (Wu *et al*, 2013). Briefly, Cas9 mRNA (100 ng/μl), sgRNA (50 ng/μl) containing *Rabl2* targeting sequence (5′ GCAUGCUCUG GAACCGCUCC 3′), and 120-nucleotide single-stranded DNA donor (100 ng/μl; 5′ CCCTCAACCC CCA GAGTTGT GTTCTTGTTG CAGACTTCTG GGATACAGCA GGCTTG GAGC GGTTCCAGAG CATGCATGCT TCCTACTACC ACAAGGCTCA CGCCTGCATC ATGGTATGAA 3′) were co-injected into the cytoplasm of fertilized C57BL/6 eggs. The injected eggs were cultured in KSOM medium to the two-cell stage and then transplanted into the uterus of pseudopregnant ICR female mice. The neonatal mice were obtained through the cesarean section at E18.5. For genotyping, a 340-bp *Rabl2* fragment covering the mutation site was PCR amplified using mouse-tail genomic DNA as template and then subjected to sequencing. The sequences of the PCR primers were 5′ GGTT CTCTCC CTCCACTTAC 3′ and 5′ GGTAGCGGGC TGAGGACCAT 3′.

## Cell culture, viral production, and transfection

HEK293T cells and HEK293A were maintained in DMEM medium (Hyclone) supplemented with 10% FBS (Biochrom), 100 U/ml penicillin (Thermo Fisher), 100 mg/ml streptomycin (Thermo Fisher), and 0.3 mg/ml ʟ-glutamine (Sigma). hTERT-RPE1 and IMCD3 cells were maintained in DMEM/F12 medium (GE Healthcare) supplemented with 10% FBS, 100 U/ml penicillin, 100 mg/ml streptomycin, and 0.3 mg/ml ʟ-glutamine. Additionally, hygromycin B (10 μg/ml; Thermo Fisher) was added into the RPE1 culture medium. Cultured cells were routinely tested for mycoplasma contamination. Primary MEFs were prepared from E12.5 mouse embryos and cultured in DMEM medium supplemented with 10% FBS, 100 U/ml penicillin, 100 mg/ml streptomycin, and 0.3 mg/ml ʟ-glutamine. MEFs cultured for less than six passages were used in experiments. To induce primary cilia formation, culture medium was replaced with serum starvation medium (DMEM with 0.25% FBS for MEFs or DMEM/F12 for RPE1 and IMCD3 cells) for 48 h. To activate Shh signaling, cells were serum-starved for 24 h and then

treated with 100 nM of SAG (566661, Millipore) for another 24 h. mTECs and mEPCs were isolated and cultured as described previously (Cao *et al*, 2012; Delgehyr *et al*, 2015; Zheng *et al*, 2019).

To express exogenous proteins, HEK293T cells were transfected using polyethylenimine (PEI 23966-2, Polysciences). IMCD3 and PRE1 cells were transfected using lipofectamine 2000 (Life Technologies). Lentiviral production was performed as described (Zhao *et al*, 2013). MEFs were infected by culturing in the 1:1 mixture of lentivirus-containing medium and fresh culture medium for 24 h and then in culture medium for another 24 h. To produce adenovirus, the plasmids were first digested with Pac I overnight. The linearized plasmids were purified by gel extraction and then transfected into HEK293A cells with Lipofectamine 2000. After approximately 80% cells showed a cytopathic effect (CPE), the cells were harvested and viral particles were released by three freeze-and-thaw (−80°C to 37°C) cycles. The harvested adenoviral particles were used for infection at a 1:1,000 dilution.

## Cilia purification and label-free quantitative mass spectrometry

Purification of ependymal cilia and label-free quantitative (LFQ) mass spectrometric analyses were carried out as described (Zhang *et al*, 2019; Zheng *et al*, 2019). For each preparation, two 75-cm$^2$ flasks of ependymal cells derived from 10 P0 mice were harvested at day 10 post-serum starvation. Purification of ependymal cilia was performed (Fig 4D) as described (Zheng *et al*, 2019). The purified cilia were lysed in 100 μl of lysis buffer (20 mM Tris–HCl [pH 7.5], 100 mM KCl, 0.1% NP-40, 1 mM EDTA, 10 mM $Na_4O_7P_2$, and protease inhibitors) and boiled for 10 min. 5 μl of the lysate was loaded for immunoblotting. For LFQ mass spectrometry (Zhu *et al*, 2010), 50 μl of each preparation was used. Ciliary proteomes identified by the LFQ mass spectrometry (related to Fig 5B) are provided in the Source Data for Fig 5.

## Microscopy

Fluorescence microscopy was carried out as described previously (Cao *et al*, 2012; Zhao *et al*, 2019). MEF and RPE1 cells were fixed with 4% paraformaldehyde in PBS. To better visualize primary cilia, cells were kept on ice for 30 min before fixation to destabilize cytoplasmic microtubules. GFP-tagged Rabl2 and mutants were immunostained with anti-GFP antibody and Alexa 488-conjugated secondary antibody to visualize ciliary localization. For immunofluorescence of mouse trachea and kidney, wild-type and *Rabl2^−/−^* mice of 2-month-old were firstly perfusion-fixed with 4% paraformaldehyde in PBS and then fixed with 4% paraformaldehyde in PBS overnight at 4°C. The kidneys of E18.5 wild-type and *Rabl2^KI/KI^* mice were dissected and fixed with 4% paraformaldehyde in PBS for 2 h at 4°C. The samples were subsequently equilibrated with 30% sucrose in PBS overnight at 4°C, embedded in OCT Tissue Freezing Medium (NE-50^TM^, Thermo Fisher) and sectioned into 10-μm slices. The cryo-sections were blocked in PBS with 10% goat serum and 0.5% Triton X-100 at room temperature for 1 h, followed by overnight incubation with primary antibodies at 4°C. Confocal images were captured using a Leica TCS SP8 system with a 63×/ 1.40 oil immersion objective and processed with maximum intensity projections. 3D-SIM super-resolution images were taken with a DeltaVision OMX SR system (GE Healthcare) with a 100×/1.40 oil

immersion objective (Olympus). Immersion oil with a refractive index of 1.516 was used to obtain optimal images and serial *z*-stack optical sectioning was set at 125-nm intervals. Images were reconstructed by softWoRx 5.0 software (GE Healthcare). Antibodies used are listed in Appendix Table S1.

## Live-cell imaging

For live-cell imaging, cells were seeded in 35-mm glass-bottom dishes (D35-20-1.5-N, Cellvis). For imaging ciliary motility of 3NG-Rabl2 or GFP-Rabl2$^{D73GQ80L}$, RPE1 cells were transfected with lentiviral plasmids for 24 h, followed by a 48-h serum starvation. Ciliary images were captured at 200-ms intervals for 30 s with a Leica DMi8 TIRF microscope equipped with a 100×/1.47 oil immersion objective. For imaging ciliary motility of 3NG-Bbs5 or Ift27-GFP, IMCD3 cells were co-transfected with lentiviral plasmids to co-express RFP-Rabl2 or RFP-Rabl2$^{Q80L}$. The cells were transfected for 24 h, followed by a 48-h serum starvation. Ciliary images were captured at 250-ms intervals for 25 s with a Zeiss LSM 880 Airyscan microscope equipped with a 63×/1.4 oil immersion objective.

Kymographs were generated from the time-lapse image sequence with KymographClear 2.0 of Image J (Fiji). Particle velocities were measured as described (Ishikawa & Marshall, 2015). Traffic frequencies were measured from kymographs as the number of particles crossing ciliary middle line per min. Particle processivity was quantified from kymographs for events lasting for > 3 s (Ye *et al*, 2018).

## Fluorescence loss in photobleaching assay

Fluorescence loss in photobleaching assays were performed as described (Snapp *et al*, 2003; Esposito *et al*, 2009; Wustner *et al*, 2012; Liew *et al*, 2014) with modifications. RPE1 cells were transfected with lentiviral plasmids to co-express 3NG-Bbs5 with RFP-tagged Rabl2 or mutants for 24 h, followed by serum starvation for 48 h to induce ciliogenesis. The cytoplasmic fluorescence of 3NG-Bbs5 around the ciliary base was photobleached in multiple areas with a 488-nm laser prior to imaging. Ciliary images were captured at 30-s intervals for up to 30 frames with a laser confocal microscope (Leica SP8) equipped with a 63×/1.4 oil immersion objective. Fluorescent intensities of ciliary 3NG-Bbs5 following time were measured with Adobe Photoshop.

## Skeletal staining and H&E staining

Skeletal staining was performed as described previously (Zou *et al*, 2013) with some modifications. All steps were performed at room temperature. Eviscerated and skinned neonates were fixed in 95% ethanol overnight, transferred into acetone for degreasing, and stained with Alizarin red/Alcian blue for 4 days. After three times of wash with 95% ethanol, soft tissues were cleared in 1% potassium hydroxide. Specimens were imaged with an Olympus SZX16 stereo microscope.

Eyes from P0 and 9-month-old *wild-type* or *Rabl2$^{-/-}$* mice and kidneys from E18.5 *wild-type* or *Rabl2$^{KI/KI}$* mice were dissected and fixed in Bouin's solution overnight at 4°C. The fixed tissues were paraffin-embedded and sectioned into 8-μm-thick slices with a microtome (Leica RM2235). The sections were deparaffinized with xylene, rehydrated, and stained with hematoxylin for 5 min and

eosin for 1 min. The images of eye sections were captured with an Olympus BX51 microscope. The images of kidney sections were captured with a Zeiss Axio Scan.Z1 Slide Scanner equipped with a 10× objective.

## Sperm motility assay

Epididymal sperms from 8-week-old *Rabl2$^{+/+}$* or *Rabl2$^{-/-}$* mice were incubated in 500 μl of sperm analysis buffer (120 mM NaCl, 20 mM KCl, 1 mM CaCl$_2$, 25 mM NaHCO$_3$, 1.2 mM MgSO$_4$, 0.36 mM NaH$_2$PO$_4$, 5.5 mM Glucose, 0.45 mM Na-Pyruvate, 20 mM Sucrose, 10 mM TAPSO, 57 mg/l Penicillin, 29 mg/l Streptomycin, pH 7.4) at 37°C for 30 min, and a 5-μl aliquot was used for the motility analysis with a computer-assisted semen analysis machine (TOX IVOS Sperm Analyzer, Hamilton Thorne).

## Scanning electron microscopy

Ependymal, tracheal, and kidney tissues from 2-month-old mice were fixed with 2.5% glutaraldehyde in PBS overnight at 4°C, post-fixed with 1% OsO$_4$ in PBS on ice for 1 h, and dehydrated with a graded ethanol series (30, 50, 70, 80, 95, 100%). Critical point drying was carried out before metal shadowing. Specimens were imaged with a scanning electron microscope (FEI Quanta 250).

## Sucrose gradient centrifugation

Testes from two 8-week-old mice were homogenized in 600 μl of lysis buffer (20 mM Tris–HCl [pH 7.5], 100 mM KCl, 0.1% NP-40, 1 mM EDTA, 10 mM Na$_4$P$_2$O$_7$, 10% glycerol, and a cocktail of proteinase inhibitors [539134, Millipore]). The lysates were cleared by centrifugation at 16,000 *g* for 20 min at 4°C. 200 μl supernatants were incubated with 1 mM GTPγS or DMSO for 1 h at 30°C. After incubation, the lysates were loaded on top of a 5-ml 10–40% continuous sucrose gradient and centrifugated at 100,000 *g* for 20 h at 4°C. 200-μl fractions were collected from top to bottom for immunoblotting.

## Immunoprecipitation and GST pull down

Co-immunoprecipitation was performed as described previously (Zhao *et al*, 2013). NIH3T3 cells infected with lentivirus to stably express GFP-tagged Rabl2, Rabl2$^{Q80L}$, or Rabl2$^{S35N}$ were serum-starved for 48 h before harvest, whereas cultured mEPCs were infected with adenovirus at 1 day before serum starvation and harvested at day 7 post-serum starvation. The cells were lysed in ice-cold lysis buffer (20 mM Tris–HCl [pH 7.5], 0.1% NP-40, 100 mM KCl, 50 mM NaF, 10 mM Na-Pyrophosphate, 1 mM Na$_3$VO$_4$, 1 mM EDTA, 10% Glycerol, 1 mM DTT, 1 mM PMSF, and protease inhibitors cocktail). The lysates were cleared by centrifugation at 16,000 *g* for 20 min at 4°C. The supernatants were incubated with anti-GFP beads (gta-400, Chromotek) for 2 h at 4°C. After washing, the beads were boiled in SDS-loading buffer for immunoblotting.

For GST pull-down assays, bacterial lysates expressing GST-tagged Rabl2$^{Q80L}$ and Rabl2$^{S35N}$ were incubated with Glutathione-agarose (G4510, Sigma) for 2 h at 4°C. After washing, the beads were incubated with bacterial lysates expressing FLAG-tagged Ift74,

Ift81, or their mixture for another 2 h. After washing, the beads were boiled in SDS-loading buffer for immunoblotting.

## Statistics

Band intensities in immunoblots and ciliary fluorescent intensities in micrographs were measured with Adobe Photoshop as described (Hoffman *et al*, 2001). Band intensities in immunoblots were normalized to the loading control. Statistical analysis was performed with paired or unpaired Student's *t*-test with GraphPad Prism 6. No blinding strategy was used in this study.

# Data availability

This study includes no data deposited in external repositories. The proteomic results of isolated cilia (Fig 5B) are provided as source data for Fig 5.

**Expanded View** for this article is available online.

## Author contributions

XZ and XY conceived and directed the project; SD, HL performed major experiments; YZ initiated this project; SY and JL generated KI mice; YC purified mEPC cilia; BQ maintained KI mouse line; CH assisted in live imaging; JW produced the Rabl2 antibody; XZ, XY, SD, YZ and HL designed experiments, interpreted data, and wrote the paper.

## Conflict of interest

The authors declare that they have no conflict of interest.

# References

Bangs F, Anderson KV (2017) Primary cilia and mammalian hedgehog signaling. *Cold Spring Harb Perspect Biol* 9: a028175

Berbari NF, O'Connor AK, Haycraft CJ, Yoder BK (2009) The primary cilium as a complex signaling center. *Curr Biol* 19: R526−R535

Bhogaraju S, Taschner M, Morawetz M, Basquin C, Lorentzen E (2011) Crystal structure of the intraflagellar transport complex 25/27. *EMBO J* 30: 1907−1918

Blacque OE, Scheidel N, Kuhns S (2018) Rab GTPases in cilium formation and function. *Small GTPases* 9: 76−94

Briscoe J, Therond PP (2013) The mechanisms of Hedgehog signalling and its roles in development and disease. *Nat Rev Mol Cell Biol* 14: 416−429

Cao J, Shen Y, Zhu L, Xu Y, Zhou Y, Wu Z, Li Y, Yan X, Zhu X (2012) miR-129-3p controls cilia assembly by regulating CP110 and actin dynamics. *Nat Cell Biol* 14: 697−706

Chen JK, Taipale J, Young KE, Maiti T, Beachy PA (2002) Small molecule modulation of Smoothened activity. *Proc Natl Acad Sci USA* 99: 14071−14076

Chou HT, Apelt L, Farrell DP, White SR, Woodsmith J, Svetlov V, Goldstein JS, Nager AR, Li Z, Muller J *et al* (2019) The molecular architecture of native BBSome obtained by an integrated structural approach. *Structure* 27: 1384−1394.e1384

D'Cruz R, Stronks K, Rowan CJ, Rosenblum ND (2020) Lineage-specific roles of hedgehog-GLI signaling during mammalian kidney development. *Pediatric Nephrology* 35: 725−731

Dateyama I, Sugihara Y, Chiba S, Ota R, Nakagawa R, Kobayashi T, Itoh H (2019) RABL2 positively controls localization of GPCRs in mammalian primary cilia. *J Cell Sci* 132: jcs224428

Delgehyr N, Meunier A, Faucourt M, Bosch Grau M, Strehl L, Janke C, Spassky N (2015) Ependymal cell differentiation, from monociliated to multiciliated cells. *Methods Cell Biol* 127: 19−35

Desai PB, San Agustin JT, Stuck MW, Jonassen JA, Bates CM, Pazour GJ (2018) Ift25 is not a cystic kidney disease gene but is required for early steps of kidney development. *Mech Dev* 151: 10−17

Eguether T, San Agustin JT, Keady BT, Jonassen JA, Liang Y, Francis R, Tobita K, Johnson CA, Abdelhamed ZA, Lo CW *et al* (2014) IFT27 links the BBSome to IFT for maintenance of the ciliary signaling compartment. *Dev Cell* 31: 279−290

Esposito A, Schlachter S, Schierle GS, Elder AD, Diaspro A, Wouters FS, Kaminski CF, Iliev AI (2009) Quantitative fluorescence microscopy techniques. *Methods Mol Biol* 586: 117−142

Forsythe E, Beales PL (2013) Bardet-Biedl syndrome. *Eur J Hum genet* 21: 8−13

Garcia-Gonzalo FR, Reiter JF (2017) Open sesame: how transition fibers and the transition zone control ciliary composition. *Cold Spring Harb Perspect Biol* 9: a028134

Goetz SC, Anderson KV (2010) The primary cilium: a signalling centre during vertebrate development. *Nat Rev Genet* 11: 331−344

He M, Subramanian R, Bangs F, Omelchenko T, Liem Jr KF, Kapoor TM, Anderson KV (2014) The kinesin-4 protein Kif7 regulates mammalian Hedgehog signalling by organizing the cilium tip compartment. *Nat Cell Biol* 16: 663−672

Hilgendorf KI, Johnson CT, Jackson PK (2016) The primary cilium as a cellular receiver: organizing ciliary GPCR signaling. *Curr Opin Cell Biol* 39: 84−92

Hirano T, Katoh Y, Nakayama K (2017) Intraflagellar transport-A complex mediates ciliary entry and retrograde trafficking of ciliary G protein-coupled receptors. *Mol Biol Cell* 28: 429−439

Hoffman DB, Pearson CG, Yen TJ, Howell BJ, Salmon ED (2001) Microtubule-dependent changes in assembly of microtubule motor proteins and mitotic spindle checkpoint proteins at PtK1 kinetochores. *Mol Biol Cell* 12: 1995−2009

Hui CC, Joyner AL (1993) A mouse model of greig cephalopolysyndactyly syndrome: the extra-toesJ mutation contains an intragenic deletion of the Gli3 gene. *Nat Genet* 3: 241−246

Hui CC, Slusarski D, Platt KA, Holmgren R, Joyner AL (1994) Expression of three mouse homologs of the *Drosophila* segment polarity gene cubitus interruptus, Gli, Gli-2, and Gli-3, in ectoderm- and mesoderm-derived tissues suggests multiple roles during postimplantation development. *Dev Biol* 162: 402−413

Hui CC, Angers S (2011) Gli proteins in development and disease. *Annu Rev Cell Dev Biol* 27: 513−537

Hwang SH, White KA, Somatilaka BN, Shelton JM, Richardson JA, Mukhopadhyay S (2018) The G protein-coupled receptor Gpr161 regulates

forelimb formation, limb patterning and skeletal morphogenesis in a primary cilium-dependent manner. *Development* 145: dev154054

Ishikawa H, Marshall WF (2011) Ciliogenesis: building the cell's antenna. *Nat Rev Mol Cell Biol* 12: 222–234

Ishikawa H, Marshall WF (2015) Efficient live fluorescence imaging of intraflagellar transport in mammalian primary cilia. *Methods Cell Biol* 127: 189–201

Jiang J, Promchan K, Jiang H, Awasthi P, Marshall H, Harned A, Natarajan V (2016) Depletion of BBS protein LZTFL1 affects growth and causes retinal degeneration in mice. *J Genet Genomics* 43: 381–391

Kanie T, Abbott KL, Mooney NA, Plowey ED, Demeter J, Jackson PK (2017) The CEP19-RABL2 GTPase complex binds IFT-B to initiate intraflagellar transport at the ciliary base. *Dev Cell* 42: 22–36.e12

Keady BT, Samtani R, Tobita K, Tsuchya M, San Agustin JT, Follit JA, Jonassen JA, Subramanian R, Lo CW, Pazour GJ (2012) IFT25 links the signal-dependent movement of Hedgehog components to intraflagellar transport. *Dev Cell* 22: 940–951

Kong JH, Siebold C, Rohatgi R (2019) Biochemical mechanisms of vertebrate hedgehog signaling. *Development* 146: dev166892

Liew GM, Ye F, Nager AR, Murphy JP, Lee JS, Aguiar M, Breslow DK, Gygi SP, Nachury MV (2014) The intraflagellar transport protein IFT27 promotes BBSome exit from cilia through the GTPase ARL6/BBS3. *Dev Cell* 31: 265–278

Lo JC, Jamsai D, O'Connor AE, Borg C, Clark BJ, Whisstock JC, Field MC, Adams V, Ishikawa T, Aitken RJ *et al* (2012) RAB-like 2 has an essential role in male fertility, sperm intra-flagellar transport, and tail assembly. *PLoS Genet* 8: e1002969

Lo JCY, O'Connor AE, Andrews ZB, Lo C, Tiganis T, Watt MJ, O'Bryan MK (2016) RABL2 is required for hepatic fatty acid homeostasis and its dysfunction leads to steatosis and a diabetes-like state. *Endocrinology* 157: 4732–4743

Lucker BF, Miller MS, Dziedzic SA, Blackmarr PT, Cole DG (2010) Direct interactions of intraflagellar transport complex B proteins IFT88, IFT52, and IFT46. *J Biol Chem* 285: 21508–21518

Milenkovic L, Weiss LE, Yoon J, Roth TL, Su YS, Sahl SJ, Scott MP, Moerner WE (2015) Single-molecule imaging of Hedgehog pathway protein Smoothened in primary cilia reveals binding events regulated by Patched1. *Proc Natl Acad Sci USA* 112: 8320–8325

Mourao A, Nager AR, Nachury MV, Lorentzen E (2014) Structural basis for membrane targeting of the BBSome by ARL6. *Nat Struct Mol Biol* 21: 1035–1041

Mourao A, Christensen ST, Lorentzen E (2016) The intraflagellar transport machinery in ciliary signaling. *Curr Opin Struct Biol* 41: 98–108

Mukhopadhyay S, Wen X, Ratti N, Loktev A, Rangell L, Scales SJ, Jackson PK (2013) The ciliary G-protein-coupled receptor Gpr161 negatively regulates the Sonic hedgehog pathway via cAMP signaling. *Cell* 152: 210–223

Nachury MV (2018) The molecular machines that traffic signaling receptors into and out of cilia. *Curr Opin Cell Biol* 51: 124–131

Nakamura N, Rabouille C, Watson R, Nilsson T, Hui N, Slusarewicz P, Kreis TE, Warren G (1995) Characterization of a cis-Golgi matrix protein, GM130. *J Cell Biol* 131: 1715–1726

Nakayama K, Katoh Y (2018) Ciliary protein trafficking mediated by IFT and BBSome complexes with the aid of kinesin-2 and dynein-2 motors. *J Biochem* 163: 155–164

Niewiadomski P, Niedziolka SM, Markiewicz L, Uspienski T, Baran B, Chojnowska K (2019) Gli proteins: regulation in development and cancer. *Cells* 8: 147

Nishimura DY, Fath M, Mullins RF, Searby C, Andrews M, Davis R, Andorf JL, Mykytyn K, Swiderski RE, Yang B *et al* (2004) Bbs2-null mice have neurosensory deficits, a defect in social dominance, and retinopathy associated with mislocalization of rhodopsin. *Proc Natl Acad Sci USA* 101: 16588–16593

Nishijima Y, Hagiya Y, Kubo T, Takei R, Katoh Y, Nakayama K (2017) RABL2 interacts with the intraflagellar transport-B complex and CEP19 and participates in ciliary assembly. *Mol Biol Cell* 28: 1652–1666

Pal K, Hwang SH, Somatilaka B, Badgandi H, Jackson PK, DeFea K, Mukhopadhyay S (2016) Smoothened determines beta-arrestin-mediated removal of the G protein-coupled receptor Gpr161 from the primary cilium. *J Cell Biol* 212: 861–875

Santos N, Reiter JF (2014) A central region of Gli2 regulates its localization to the primary cilium and transcriptional activity. *J Cell Sci* 127: 1500–1510

Seo S, Zhang Q, Bugge K, Breslow DK, Searby CC, Nachury MV, Sheffield VC (2011) A novel protein LZTFL1 regulates ciliary trafficking of the BBSome and Smoothened. *PLoS Genet* 7: e1002358

Shaner NC, Lambert GG, Chammas A, Ni Y, Cranfill PJ, Baird MA, Sell BR, Allen JR, Day RN, Israelsson M *et al* (2013) A bright monomeric green fluorescent protein derived from Branchiostoma lanceolatum. *Nat Methods* 10: 407–409

Shelton KR, Egle PM, Cochran DL (1981) Nuclear envelope proteins: identification of lamin B subtypes. *Biochem Biophys Res Comm* 103: 975–981

Siljee JE, Wang Y, Bernard AA, Ersoy BA, Zhang SM, Marley A, Von Zastrow M, Reiter JF, Vaisse C (2018) Subcellular localization of MC4R with ADCY3 at neuronal primary cilia underlies a common pathway for genetic predisposition to obesity. *Nat Genet* 50: 180–185

Snapp EL, Altan N, Lippincott-Schwartz J (2003) Measuring protein mobility by photobleaching GFP chimeras in living cells. *Curr Protoc Cell Biol* Chapter 21: Unit 21 21

Stenmark H (2009) Rab GTPases as coordinators of vesicle traffic. *Nat Rev Mol Cell Biol* 10: 513–525

Tadenev AL, Kulaga HM, May-Simera HL, Kelley MW, Katsanis N, Reed RR (2011) Loss of Bardet-Biedl syndrome protein-8 (BBS8) perturbs olfactory function, protein localization, and axon targeting. *Proc Natl Acad Sci USA* 108: 10320–10325

Taschner M, Kotsis F, Braeuer P, Kuehn EW, Lorentzen E (2014) Crystal structures of IFT70/52 and IFT52/46 provide insight into intraflagellar transport B core complex assembly. *J Cell Biol* 207: 269–282

Tickle C, Towers M (2017) Sonic Hedgehog signaling in limb development. *Front Cell Dev Biol* 5: 14

Wang B, Fallon JF, Beachy PA (2000) Hedgehog-regulated processing of Gli3 produces an anterior/posterior repressor gradient in the developing vertebrate limb. *Cell* 100: 423–434

Wang WJ, Tay HG, Soni R, Perumal GS, Goll MG, Macaluso FP, Asara JM, Amack JD, Tsou MF (2013) CEP162 is an axoneme-recognition protein promoting ciliary transition zone assembly at the cilia base. *Nat Cell Biol* 15: 591–601

Wu Y, Liang D, Wang Y, Bai M, Tang W, Bao S, Yan Z, Li D, Li J (2013) Correction of a genetic disease in mouse via use of CRISPR-Cas9. *Cell Stem Cell* 13: 659–662

Wustner D, Solanko LM, Lund FW, Sage D, Schroll HJ, Lomholt MA (2012) Quantitative fluorescence loss in photobleaching for analysis of protein transport and aggregation. *BMC Bioinformatics* 13: 296

Xu Y, Cao J, Huang S, Feng D, Zhang W, Zhu X, Yan X (2015) Characterization of tetratricopeptide repeat-containing proteins critical for cilia formation and function. *PLoS One* 10: e0124378

Yang TT, Su J, Wang WJ, Craige B, Witman GB, Tsou MF, Liao JC (2015) Superresolution pattern recognition reveals the architectural map of the ciliary transition zone. *Sci Rep* 5: 14096

Ye F, Breslow DK, Koslover EF, Spakowitz AJ, Nelson WJ, Nachury MV (2013) Single molecule imaging reveals a major role for diffusion in the exploration of ciliary space by signaling receptors. *eLife* 2: e00654

Ye F, Nager AR, Nachury MV (2018) BBSome trains remove activated GPCRs from cilia by enabling passage through the transition zone. *J Cell Biol* 217: 1847–1868

Zhang Q, Nishimura D, Vogel T, Shao J, Swiderski R, Yin T, Searby C, Carter CS, Kim G, Bugge K *et al* (2013) BBS7 is required for BBSome formation and its absence in mice results in Bardet-Biedl syndrome phenotypes and selective abnormalities in membrane protein trafficking. *J Cell Sci* 126: 2372–2380

Zhang Y, Chen Y, Zheng J, Wang J, Duan S, Zhang W, Yan X, Zhu X (2019) Vertebrate Dynein-f depends on Wdr78 for axonemal localization and is essential for ciliary beat. *J Mol Cell Biol* 11: 383–394

Zhao H, Zhu L, Zhu Y, Cao J, Li S, Huang Q, Xu T, Huang X, Yan X, Zhu X (2013) The Cep63 paralogue Deup1 enables massive de novo centriole biogenesis for vertebrate multiciliogenesis. *Nat Cell Biol* 15: 1434–1444

Zhao H, Chen Q, Fang C, Huang Q, Zhou J, Yan X, Zhu X (2019) Parental centrioles are dispensable for deuterosome formation and function during basal body amplification. *EMBO Rep* 20: e46735

Zheng J, Liu H, Zhu L, Chen Y, Zhao H, Zhang W, Li F, Xie L, Yan X, Zhu X (2019) Microtubule-bundling protein Spef1 enables mammalian ciliary central apparatus formation. *J Mol Cell Biol* 11: 67–77

Zhu W, Smith JW, Huang CM (2010) Mass spectrometry-based label-free quantitative proteomics. *J Biomed Biotechnol* 2010: 840518

Zou W, Greenblatt MB, Brady N, Lotinun S, Zhai B, de Rivera H, Singh A, Sun J, Gygi SP, Baron R *et al* (2013) The microtubule-associated protein DCAMKL1 regulates osteoblast function via repression of Runx2. *J Exp Med* 210: 1793–1806